ISSN 2096-7071 (Print)
ISSN 2097-3101 (Online)
CN 10-1629/R1

CHINA CDC WEEKLY

Vol. 8 No. 8 Feb. 20, 2026

CCDC weekly

中国疾病预防控制中心周报(英文)

Vital Surveillances

Preplanned Studies

Methods and Applications

Review

ISSN 2096-7071

China CDC Weekly

Editorial Board

Honorary Editor-in-Chief Hongbing Shen

Founding Editor-in-Chief George F. Gao

Advisory Board Member
Jianguo Xu
Liming Li
Yu Wang
Gabriel M Leung
Zijian Feng

Editor-in-Chief Jianwei Wang

Deputy Editor-in-Chief
Zhuo Chen (USA)
Zhibin Hu
Qun Li
Zhengliang Li
Xiaoming Shi
Yan Sun
Changjun Wang
Tangchun Wu
Yongning Wu
Ningshao Xia
Chihong Zhao

Editorial Board Member
Jianping Cao
Guobing Chen
Xi Chen (USA)
Gong Cheng
Gangqiang Ding
Xiaoping Dong
Pei Gao
Xin Guo
Jun Han
Mengjie Han
Weidong Hao
Na He
Yuping He
Guoqing Hu
Cunrui Huang
John S. Ji (USA)
Na Jia
Weihua Jia
Zhongwei Jia
Biao Kan
Haidong Kan
Jianqiang Lai
Lance Rodewald (USA)
Ni Li
Shizhu Li
Ying Li
Zhenjun Li
Zhongjie Li
Geyu Liang
Yuan Lin
Aidong Liu
Min Liu
Qiyong Liu
Qingjie Liu
Yawen Liu
Jinxing Lu
Xiangfeng Lu
David LYE Chien Boon (Singapore)
Fan Lyu
Jun Lyu
Huilai Ma
Jiaqi Ma
Chen Mao
Xiaoping Miao
An Pan
Jie Pan
Lili Ren
Guoqing Shi
Yuelong Shu
Chengye Sun
Quanfu Sun
Xin Sun
Hua Wang
Huaqing Wang
Hui Wang
Jianming Wang
Junling Wang
Lin Wang
Tong Wang
Shenghui Wu (USA)
Min Xia
Lin Xiao
Dongqun Xu
Hongyan Yao
Guojing Yang
Zundong Yin
Dianke Yu
Hongjie Yu
Siyan Zhan
Jianzhong Zhang
Jun Zhang
Liubo Zhang
Tao Zhang
Yanping Zhang
Wei Zhao
Yanlin Zhao
Maigeng Zhou
Xiaonong Zhou
Yongqun Zhu
Guihua Zhuang

Editorial Office

Directing Editor Chihong Zhao

Managing Editor Yu Chen

Senior Scientific Editors
Xuejun Ma
Daxin Ni
Ning Wang
Wenwu Yin
Shicheng Yu
Jianzhong Zhang
Qian Zhu

Scientific Editors
Weihong Chen
Tao Jiang
Dongmin Li
Xudong Li
Nankun Liu
Liwei Shi
Liuying Tang
Meng Wang
Zhihui Wang
Qi Yang
Qing Yue
Lijie Zhang
Ying Zhang

Editor in Charge Meng Wang

Cover Image: credited from the designer Jiaying Wang.
This week's issue were organized by Guest Editor Zhongwei Jia.

Vital Surveillances

Genomic Insights into the 2024 HAdV-14p1 Strain in China: Traced to Early Prevalent Strains

Yali Jin[1]; Jiangxia Wang[2]; Naiying Mao[1]; Chunyu Zhu[1]; Haiqing Zhou[1]; Weiyan He[1];
Hao Ding[1]; Baicheng Xia[1]; Aili Cui[1]; Yan Zhang[1]; Zhen Zhu[1,#]; Hongmei Xu[2,#]

ABSTRACT

Introduction: Human adenovirus type 14 variant p1 (HAdV-14p1) has been associated with severe respiratory infections worldwide. However, no cases of HAdV-14p1 infection have been reported in China since 2019. HAdV-14 was unexpectedly identified in 2024 in a pediatric patient hospitalized with bronchopneumonia in Chongqing, China. This study aims to elucidate the genetic characteristics of this strain and determine its phylogenetic relationship with previously circulating domestic and international strains.

Methods: Whole-genome sequencing was performed on the HAdV-14 strain Chongqing2024-115, followed by comprehensive phylogenetic and genetic variation analyses using all publicly available global HAdV-14 genome sequences from the GenBank database.

Results: Genome-based phylogenetic analysis classified global HAdV-14 strains into two well-supported clades: the HAdV-14 prototype clade and the variant HAdV-14p1 clade. The latter was further subdivided into three distinct subclades (I–III). Chongqing2024-115 clustered closely with earlier HAdV-14p1 subclade III and isolates from Beijing (2012) and Gansu (2013), showing high sequence identity (99.7%–99.9%). Compared with the genome of the HAdV-14 prototype strain (de Wit, AY803294), all three HAdV-14p1 subclades shared 99 specific nucleotide variations, including a six-nucleotide deletion in the knob domain of the fiber gene (nt751–756). The identification of subclade-specific variations and mutations unique to strain Chongqing2024-115 indicates ongoing microevolution within the HAdV-14p1 clade.

Conclusions: Our results confirm that the contemporary HAdV-14p1 strain shares a common genetic ancestry with earlier Chinese subclade III strains. Considering the association between HAdV-14p1 and severe disease, sustained surveillance is essential to understand better its prevalence, evolution, and impact on public health in China.

Human adenoviruses (HAdVs) are non-enveloped, double-stranded DNA viruses with a genome size of approximately 35–36 kb (*1*). To date, 117 types have been identified and classified into seven species (A–G; http://hadvwg.gmu.edu/). Due to their diverse tissue tropisms, HAdV infections are associated with various illnesses, including acute respiratory infections, gastroenteritis, and conjunctivitis (*2*). Respiratory infections are frequently associated with specific species, including B (HAdV-3, 7, 14, 21, and 55), C (HAdV-1, 2, 5, and 6), and E (HAdV-4) (*3*).

HAdV type 14 (HAdV-14) was first identified in 1955 in a military recruit with acute respiratory disease (ARD) in the Netherlands, with only limited reports documented over subsequent decades (*4*). Approximately 50 years later, a novel and highly transmissible variant, designated human adenovirus type 14 variant p1 (HAdV-14p1), emerged and triggered multiple outbreaks in several countries, including the United States, the United Kingdom, Ireland, Canada, and Japan (*5–9*). These outbreaks affected both military and civilian populations and were associated with severe and fatal ARD cases (*10*). In China, HAdV-14p1 was initially detected in Guangzhou in 2010, with subsequent outbreaks in Beijing (2012), Liaoning (2012 and 2016), Gansu (2013), and Jiangsu (2015), resulting in substantial hospitalizations (*11–15*). HAdV-14p1 was sporadically detected in other provinces between 2011 and 2019. However, since 2019, no further cases have been reported in China.

Following the COVID-19 pandemic, HAdV-14 was newly identified in 2024 through sentinel surveillance in a pediatric patient hospitalized with bronchopneumonia in Chongqing, China. To elucidate the genetic characteristics of this re-emerging HAdV-14 strain and determine its phylogenetic relationship with previously circulating domestic and international strains, we sequenced its complete genome; and performed comprehensive phylogenetic and genetic variation analyses using publicly available global HAdV-14 genome data from GenBank.

METHODS

Strain Source and Clinical Information

Sentinel surveillance for acute respiratory infections conducted since 2019 and covering 15 provinces did not detect HAdV-14 until 2024. In 2024, the HAdV-14 strain Chongqing2024-115 was isolated from a sputum sample collected from a 4-year-old male patient hospitalized with acute bronchitis in Chongqing, China. The patient presented with primary symptoms of fever, cough, and expectoration and required a 10-day hospitalization. Chest imaging revealed no significant abnormalities in either lung. Initial pathogen screening was positive for HAdV, and subsequent sequencing and analysis of the penton base, hexon, and fiber genes confirmed a HAdV-14 infection.

Genomic Sequencing and Annotation

Viral DNA was extracted from Chongqing2024-115 using a QIAamp DNA Mini Kit (Qiagen, Hilden, Germany). Whole-genome sequencing (WGS) was performed by iGeneTech Biotechnology Ltd. using a probe-based hybrid capture approach, followed by next-generation sequencing. This process yielded over 1 Gb of sequencing data, achieving complete genome coverage (100%) at a depth exceeding 8,000×. Sanger sequencing was used to validate genomic regions containing ambiguous bases. The genome was annotated using Geneious Prime software by mapping the sequences to the HAdV-14 prototype strain (de Wit, GenBank accession number AY803294). Complete genomic sequence of the Chongqing2024-115 strain in this study was deposited in the China National Microbiology Data Center with accession number NMDCN0009AD2.

Dataset

All available HAdV-14 WGSs were retrieved from GenBank. After removing incomplete and redundant sequences, a dataset of 67 WGSs from nine countries (1955–2024) was established. This dataset included five Chinese strains (2010–2013) and 62 strains from eight countries and regions (1955–2024), including the United States, Canada, Japan, Honduras, Ireland, Nepal, the Netherlands, and Scotland. With the addition of the newly sequenced strain Chongqing2024-115 from this study, a final dataset of 68 WGSs was compiled for subsequent phylogenetic and genetic variation analyses.

Bioinformatics Analyses

Sequence alignment was performed using ClustalW in MEGA v7 (http://www.megasoftware.net), followed by pairwise similarity assessment using BioEdit v7.0.4.1 (http://www.mbio.ncsu.edu/BioEdit/bioedit.html). A maximum likelihood phylogenetic tree was constructed using MEGA v7, with bootstrap support (>80%) indicated at the corresponding nodes. In addition, a phylogenetic network based on WGSs was constructed using SplitsTree v4.19.2 (http://www.splitstree.org) for viral evolutionary analysis. Genetic variations were identified using the Snipit package, focusing on nucleotide mutations at a frequency of 100%. Recombination analysis was conducted using RDP4 (http://web.cbio.uct.ac.za/~darren/rdp.html) and SimPlot v3.5.1 (http://sray.med.som.jhmi.edu/RaySoft/SimPlot) (window size, 2,000 bp; step size, 100 bp).

RESULTS

Genomic Characterization

The complete genome of Chongqing2024-115 was 34,766 bp in length, with a GC content of 48.85%, consistent with the previously reported HAdV-14 genome (*11*). Annotation using the HAdV-14 prototype strain (AY803294) as a reference identified 38 protein-coding regions (Supplementary Table S1, available at https://weekly.chinacdc.cn/). Nucleotide sequence alignment revealed 99.6% identity with the prototype strain. Further analysis of 12 key functional regions, including genes encoding major capsid proteins (penton base, hexon, and fiber), core proteins (pV, pVII, pTP, and pIVa2), minor proteins (pIX, pIIIa, pVI, and pVIII), and the non-structural protein pX, showed that, with the exception of the fiber gene region (nt, 99.1%; aa, 98.7%), the remaining 11 regions exhibited high sequence similarity compared with the prototype strain (nt, 99.6%–100.0%; aa, 99.0%–100.0%) (Table 1).

TABLE 1. Sequence identity between strain Chongqing2024-115 and the HAdV-14 prototype strain (de Wit, AY803294).

Coding regions		Identity %	
		NT	AA
Major capsid protein	penton base	99.8	99.6
	hexon	99.8	99.8
	fiber	99.1	98.7
Core protein	pV	99.9	100.0
	PVII	99.8	100.0
	pTP	99.6	99.0
	pIVa2	99.7	99.2
Minor protein	pIX	100.0	100.0
	pIIIa	99.8	100.0
	pVI	99.8	99.5
	pVIII	99.8	100.0
Non-structural protein	pX	100.0	100.0
Whole genome sequence		99.6	

Abbreviation: NT=Nucleotide; AA=Amino Acid.

Phylogenetic Analysis

To elucidate the genetic relationship between Chongqing2024-115 and previously reported domestic and international HAdV-14 strains, phylogenetic analysis was conducted using the constructed WGS dataset (Figure 1). Consistent with previous findings, all 68 strains clustered into two well-supported clades: the HAdV-14 clade, comprising the prototype strain, and the distinct HAdV-14p1 clade (*14*). Notably, the HAdV-14p1 clade could be further subdivided into three subclades (I–III; bootstrap values >80%), a finding corroborated by phylogenetic network analysis, which revealed three independent evolutionary trajectories among these strains (Supplementary Figure S1, available at https://weekly.chinacdc.cn/). Nevertheless, all three subclades exhibited high sequence identity (99.5%–99.6%) with the HAdV-14 prototype strain, indicating a highly conserved HAdV-14 genome.

Chongqing2024-115 was phylogenetically assigned to HAdV-14p1 subclade III, which also included two other Chinese strains isolated from Beijing (2012) and Gansu (2013) (intra-subclade genetic distance, 0.00065). In contrast, subclades I and II exhibited broader geographical and temporal distributions. Subclade I comprised 54 strains from six countries, including the United States, Canada, Honduras, Ireland, Nepal, and Scotland (2003–2020; intra-subclade genetic distance, 0.00005). Subclade II consisted of three Chinese strains from Guangzhou (2010) and Beijing (2011), along with five strains from the United States and Japan (2006–2024; intra-subclade genetic distance, 0.00008). High sequence identity was observed among the three subclades (genetic distance, 0.00036–0.00065), indicating a close phylogenetic relationship.

Genetic Variation

WGS-based genetic variation analysis was conducted across HAdV-14p1 subclades I–III using the HAdV-14 prototype strain as the reference genome (Supplementary Figure S2, available at https://weekly.chinacdc.cn/). Comparative genomic analysis revealed that the three subclades shared 99 specific nucleotide variations, comprising 85 single-nucleotide substitutions, six insertions, and eight deletions. These variations were distributed across the entire genome, whereas insertions and deletions were predominantly located in regions 11,000 bp upstream and 31,500 bp downstream. Subclade-specific variations were identified: subclade I harbored four substitutions and one insertion; subclade II contained six substitutions, one insertion, and one deletion; and subclade III possessed three nucleotide substitutions.

Detailed analysis of the 12 key functional regions identified 28 shared nucleotide variations across all three HAdV-14p1 subclades. These variations were distributed across 10 protein-coding regions (excluding pIX and pX), resulting in 15 amino acid changes (Figure 2). A shared six-nucleotide deletion

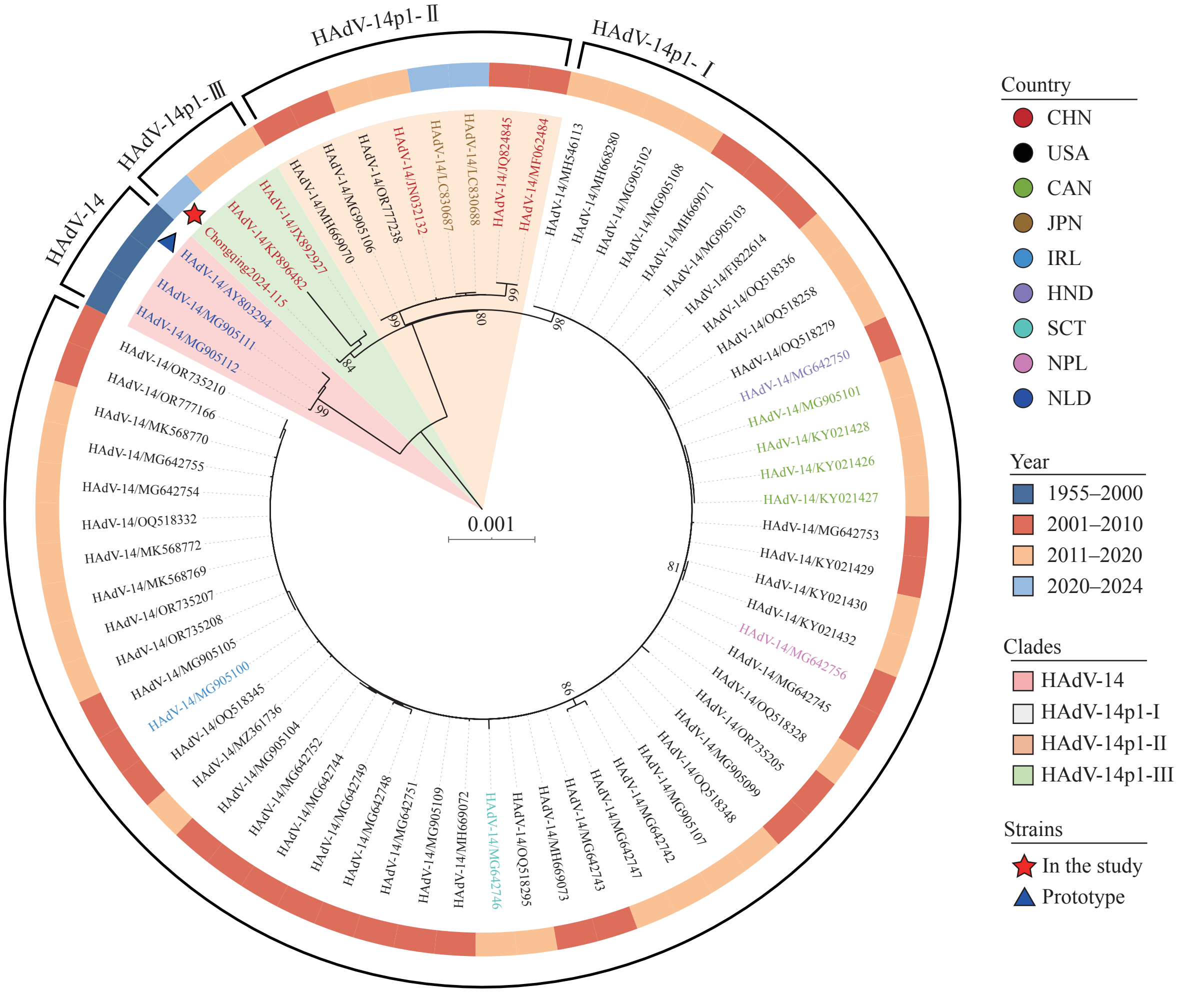

FIGURE 1. Maximum-likelihood phylogenetic tree of 68 HAdV-14 whole-genome sequences, including strain Chongqing2024-115 in this study and 67 strains from GenBank database.
Abbreviation: HAdV-14=Human adenovirus type 14.

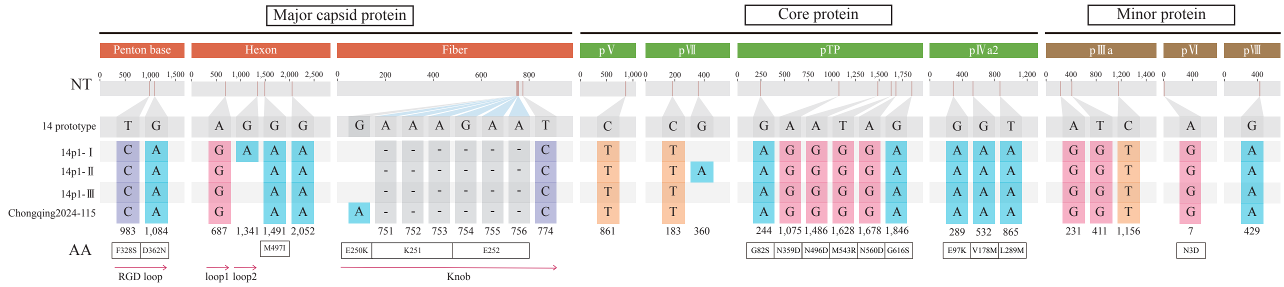

FIGURE 2. Nucleotide and amino acid variations specific to HAdV-14p1 clades and strain Chongqing2024-115 in 10 key coding regions compared to the HAdV-14 prototype strain (de Wit, AY803294).
Note: In the schematic representation, major capsid proteins are shown in orange, core proteins in green, and minor proteins in brown. The annotation “NT” denotes nucleotide variation. “-” indicates nucleotide deletion, and the “AA” row displays amino acid variations resulting from mutations. Important functional regions are marked with red arrows.

(nt751–756) within the fiber gene, located in the knob domain, resulted in the loss of two amino acids (K251 and E252). Two shared nonsynonymous variations in the penton base gene (T983C and G1084A), located within the RGD loop region, caused amino acid substitutions F328S and D362N, respectively. Subclade-specific nucleotide mutations were detected, including a synonymous mutation in the hexon gene

(G1341A) specific to subclade I and a synonymous mutation in the pVII gene (G360A) unique to subclade II. Chongqing2024-115 was characterized by two unique nucleotide substitutions: a synonymous mutation (T5601C) in the DNA polymerase gene and a nonsynonymous mutation (G31517A; E250K) within the knob region of the fiber gene (Supplementary Figure S2).

Genetic Recombination

A comprehensive recombination analysis was performed on all available HAdV-14p1 strains, including Chongqing2024-115, using WGSs from nine species B prototype strains retrieved from GenBank (recombinant strains were excluded to avoid analytical bias). The results indicated that no intra-species recombination events were detectable within the HAdV-14p1 clade.

DISCUSSION

Since 2019, no cases of HAdV-14p1 infection have been reported in China. As a highly contagious pathogen associated with substantial hospitalization and mortality, understanding the genetic origin of the recently identified HAdV-14p1 is crucial. We performed a comprehensive genomic characterization of the HAdV-14 strain Chongqing2024-115, isolated from a pediatric patient hospitalized with bronchopneumonia. Phylogenetic analysis revealed that this strain clustered closely with earlier HAdV-14p1 subclade III isolates obtained from respiratory infection outbreaks in Beijing (2012) and Gansu (2013) (*13*). The low intra-subclade genetic distance (0.00065) further supports a common evolutionary origin among these viruses, suggesting sustained transmission of this subclade within China. The absence of reported cases over the past decade may indicate prolonged cryptic transmission of this virus in the population, potentially due to factors such as insufficient surveillance efforts or the failure to systematically capture cases with mild symptoms, leading to a detection gap.

Compared with subclade III, the other two subclades (subclade I, detected across six countries during 2003–2020; subclade II, identified in three countries between 2006 and 2024) demonstrated broader spatiotemporal distributions. These subclades have maintained considerable genomic conservation over nearly two decades, as reflected by their low intra-subclade genetic distance (≤0.00065). All three subclades exhibited high sequence identity (99.5%–99.6%) with the prototype HAdV-14 strain (de Wit, 1955), and the 99 shared variations (85 substitutions, six insertions, and eight deletions) represent a conserved genetic signature of the HAdV-14p1 variant that has circulated globally since its re-emergence after an approximately 50-year absence. Notably, the six-nucleotide deletion in the fiber gene (nt751–756) resulted in a two–amino acid deletion (K251 and E252) in the knob domain. This deletion has previously been identified as a hallmark genetic characteristic distinguishing the HAdV-14p1 strain from the HAdV-14 prototype (*14*). This two–amino acid deletion has been consistently present in all globally circulating strains identified since 2003, suggesting an important role in the adaptive evolution of HAdV-14p1. Additionally, strain Chongqing2024-115 harbors a unique amino acid substitution (E250K) within the knob domain of the fiber gene. Given the critical role of this domain in mediating viral attachment to and entry into host cells, further investigation is needed to determine whether this substitution affects viral infectivity.

The subdivision of HAdV-14p1 into three distinct subclades underscores the importance of high-resolution genomic data in tracking pathogen evolution. Although the overall genetic distances between subclades were minimal (0.00036–0.00065), consistent clustering patterns suggest that subtle genetic changes may be associated with adaptive evolution or host-specific interactions. The identification of subclade-specific variations and strain-specific mutations, such as those observed in the Chongqing2024-115 isolate, indicates ongoing microevolution within the HAdV-14p1 clade. Despite the detection of subclades II and III in China since 2011, research on HAdV-14p1 remains limited, with only five relevant Chinese genomic sequences (2010–2013) available in public databases. This scarcity of genetic data constrains a comprehensive understanding of the molecular epidemiology and endemic transmission patterns of HAdV-14p1 in China. Therefore, strengthening genomic surveillance is necessary to elucidate the prevalence, evolution, and public health impact of HAdV-14p1 in China.

In conclusion, WGS-based analysis provided a detailed view of the genetic characteristics of the newly identified HAdV-14p1 strain in China in 2024. Our findings confirm that the contemporary HAdV-14p1 strain shares common genetic ancestry with earlier circulating Chinese subclade III strains. Given the association between HAdV-14p1 and severe illness, ongoing surveillance is imperative to gain a deeper understanding of its prevalence and evolution in China and to provide a basis for the formulation of targeted prevention and control measures.

Acknowledgments: The sentinel surveillance hospital in Chongqing for providing the viral strains and associated clinical data. This study used only viral strains and did not involve specimen collection.

Conflicts of interest: No conflicts of interest.

Funding: Supported by the National Key R&D Program of China (2022YFC2305303).

doi: 10.46234/ccdcw2026.033

Corresponding authors: Zhen Zhu, zhuzhen@ivdc.chinacdc.cn; Hongmei Xu, xuhongm0095@hospital.cqmu.edu.cn.

---

[1] National Key Laboratory of Intelligent Tracking and Forecasting for Infectious Disease, NHC Key Laboratory of Medical Virology and Viral Diseases, National Institute for Viral Disease Control and Prevention, Chinese Center for Disease Control and Prevention, Beijing, China; [2] Department of Infectious Diseases, Children's Hospital Affiliated to Chongqing Medical University, Chongqing, China.

Submitted: November 03, 2025
Accepted: January 19, 2026
Issued: February 20, 2026

REFERENCES

1. Davison AJ, Benkő M, Harrach B. Genetic content and evolution of adenoviruses. J Gen Virol 2003;84(Pt 11):2895-908. http://dx.doi.org/10.1099/vir.0.19497-0.
2. Mao NY, Zhu Z, Zhang Y, Xu WB. Current status of human adenovirus infection in China. World J Pediatr 2022;18(8):533 – 7. https://doi.org/10.1007/s12519-022-00568-8.
3. Liu MC, Xu Q, Li TT, Wang T, Jiang BG, Lv CL, et al. Prevalence of human infection with respiratory adenovirus in China: a systematic review and meta-analysis. PLoS Negl Trop Dis 2023;17(2):e0011151. https://doi.org/10.1371/journal.pntd.0011151.
4. Van Der Veen J, Kok G. Isolation and typing of adenoviruses recovered from military recruits with acute respiratory disease in The Netherlands. Am J Hyg 1957;65(2):119 – 29. https://doi.org/10.1093/oxfordjournals.aje.a119860.
5. Lewis PF, Schmidt MA, Lu XY, Erdman DD, Campbell M, Thomas A, et al. A community-based outbreak of severe respiratory illness caused by human adenovirus serotype 14. J Infect Dis 2009;199(10):1427 – 34. https://doi.org/10.1086/598521.
6. O'Flanagan D, O'Donnell J, Domegan L, Fitzpatrick F, Connell J, Coughlan S, et al. First reported cases of human adenovirus serotype 14p1 infection, Ireland, October 2009 to July 2010. Euro Surveill 2011;16(8):19801. https://pubmed.ncbi.nlm.nih.gov/21371411/.
7. Girouard G, Garceau R, Thibault L, Oussedik Y, Bastien N, Li Y. Adenovirus serotype 14 infection, New Brunswick, Canada, 2011. Emerg Infect Dis 2013;19(1):119 – 22. https://doi.org/10.3201/eid1901.120423.
8. Parcell BJ, McIntyre PG, Yirrell DL, Fraser A, Quinn M, Templeton K, et al. Prison and community outbreak of severe respiratory infection due to adenovirus type 14p1 in Tayside, UK. J Public Health (Oxf) 2015;37(1):64 – 9. https://doi.org/10.1093/pubmed/fdu009.
9. Mizuno S, Tanimoto Y, Mori A, Fuseya T, Ishida Y, Nishiyama M, et al. Acute encephalopathy associated with human adenovirus type 14 infection in 7-year-old girl, Japan. Emerg Infect Dis 2025;31(2):377 – 9. https://doi.org/10.3201/eid3102.241168.
10. Carr MJ, Kajon AE, Lu XY, Dunford L, O'Reilly P, Holder P, et al. Deaths associated with human adenovirus-14p1 infections, Europe, 2009-2010. Emerg Infect Dis 2011;17(8):1402 – 8. https://doi.org/10.3201/eid1708.101760.
11. Zhang QW, Seto D, Zhao SH, Zhu L, Zhao W, Wan CS. Genome sequence of the first human adenovirus type 14 isolated in China. J Virol 2012;86(12):7019 – 20. https://doi.org/10.1128/jvi.00814-12.
12. Huang GH, Yu DS, Zhu Z, Zhao H, Wang P, Gray GC, et al. Outbreak of febrile respiratory illness associated with human adenovirus type 14p1 in Gansu Province, China. Influenza Other Respir Viruses 2013;7(6):1048 – 54. https://doi.org/10.1111/irv.12118.
13. Mi ZQ, Butt AM, An XP, Jiang T, Liu W, Qin CF, et al. Genomic analysis of HAdV-B14 isolate from the outbreak of febrile respiratory infection in China. Genomics 2013;102(5-6):448 – 55. https://doi.org/10.1016/j.ygeno.2013.09.001.
14. Liao LN, Chen YH, Wang YY, Ren RW, Li J, Zhang S, et al. Genomic characteristics and phylogenetic analysis of human adenovirus 14 in China during 2010-2016. Infect Genet Evol 2025;134:105805. https://doi.org/10.1016/j.meegid.2025.105805.
15. Zhu WW, Wu WW, Xu YP, Du YG, Tang LY, Tong J. Epidemiological characteristics and genotypes of human adenovirus among children in Xuzhou from 2013 to 2017. Int J Virol 2018;25(5):315 – 8. https://doi.org/10.3760/cma.j.issn.1673-4092.2018.05.008.

SUPPLEMENTARY MATERIAL

SUPPLEMENTARY TABLE S1. Genomic annotations of strain Chongqing2024-115.

Gene	Encoded product	Chongqing2024-115
E1A	29.1 kDa protein	563-1,142; 1,227-1,435
	6.5 kDa protein	563-634; 1,227-1,331
E1B	20 kDa protein	1,605-2,147
	54.9 kDa protein	1,910-3,394
IX	pIX protein	3,477-3,896
IVa2	IVa2 protein	3,963-5,296; 5,575-5,587
E2B	DNA polymerase	5,066-8,638; 13,625-13,633
	terminal protein precursor	8,437-10,398; 13,625-13,633
L1	43 kDa protein	10,649-11,809
	protein IIIa precursor	11,835-13,599
L2	penton protein	13,681-15,357
	protein VII	15,362-15,940
	protein V precursor	15,983-17,038
	protein X	17,067-17,297
L3	protein VI	17,378-18,118
	hexon protein	18,234-21,071
	23 kDa protein	21,108-21,737
E2A	DNA binding protein	21,815-23,371
L4	100 kDa hexon-assembly associated protein	23,402-25,840
	33 kDa protein	25,572-25,890; 26,060-26,421
	22 kDa protein	25,572-26,147
	protein VIII	26,471-27,154
E3	11.7 kDa protein	27,154-27,471
	14.6 kDa protein	27,425-27,820
	18.4 kDa protein	27,805-28,305
	20.1 kDa protein	28,325-28,870
	20.8 kDa protein	28,888-29,439
	10.1 kDa protein	29,483-29,758
	14.9 kDa protein	29,763-30,167
	15 kDa protein	30,160-30,567
U	U protein	30,591-30,755
L5	fiber protein	30,770-31,741
E4	Orf6/7 protein	31,777-32,028; 32,751-32,924
	Orf6 protein	32,025-32,924
	Orf4 protein	32,827-33,195
	Orf3 protein	33,204-33,557
	Orf2 protein	33,554-33,943
	Orf1 protein	33,986-34,363

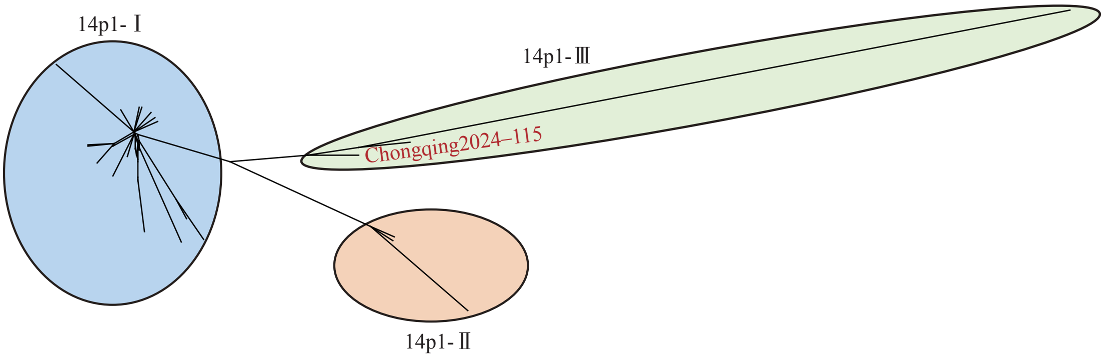

SUPPLEMENTARY FIGURE S1. Phylogenetic network generated based on WGS of 65 HAdV-14p1 strains.
Abbreviation: WGS=Whole Genome Sequence; HAdV-14=Human adenovirus type 14.

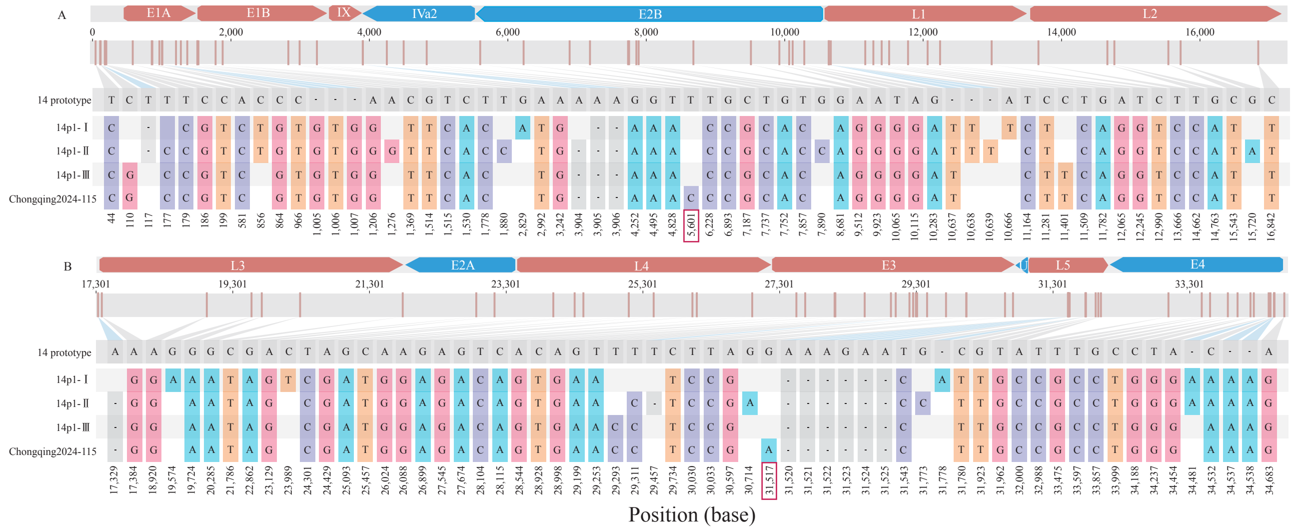

SUPPLEMENTARY FIGURE S2. Nucleotide variations specific to HAdV-14p1 clades and strain Chongqing2024-115 in the whole genome compared to the HAdV-14 prototype strain (de Wit, AY803294). (A) The genomic fragment 1–17,300 bp; (B) The fragment 17,301 bp to the end.
Notes: "-" indicates nucleotide deletion; variation sites unique to the strain Chongqing 2024-115 are highlighted with red boxes.

Preplanned Studies

Integrated Risk Matrix and Borda Count Analysis on Importation Risk Assessment of Nipah Virus Infection — China, 1999–2026

Weijing Shang[1,2]; Qiwen Zheng[1,2,#]

Summary

What is already known about this topic?

Nipah virus (NiV) is a highly lethal zoonotic pathogen. Its re-emergence in India in early 2026 has heightened global public health concerns.

What is added by this report?

This study systematically assessed the risk of NiV importation into China from five affected countries. India and Bangladesh posed moderate importation risks, whereas Malaysia, the Philippines, and Singapore presented low risks.

What are the implications for public health practice?

The findings emphasize that coupling existing defenses with sustained multi-source surveillance and dynamic risk modeling is essential to mitigate risks of stochastic NiV entry.

Abstract

Introduction: Nipah virus (NiV) infection is a highly fatal zoonosis lacking specific vaccines or treatments, posing a persistent threat to global health security; its re-emergence in India in early 2026 has further amplified these concerns. However, the risk of NiV importation into China remains unclear.

Methods: This study employed an integrated risk matrix and Borda count method, driven by multisectoral data including epidemiological parameters, civil aviation capacity, customs import trade, and geographical proximity. Importation risk was evaluated across two dimensions: likelihood and consequences. The Borda count method was subsequently utilized to rank the comprehensive risks among identified affected countries.

Results: Importation risk from five countries reporting NiV outbreaks between 1999 and 2026 was evaluated by scoring and ranking both likelihood and consequences. India and Bangladesh presented moderate importation risk to China, achieving the highest Borda points among South and Southeast Asian nations. Malaysia, the Philippines, and Singapore demonstrated low importation risk.

Conclusions: Countries with documented NiV outbreaks represent potential sources of importation to China, where stochastic viral entry poses a persistent threat in an increasingly interconnected world. Continuous multi-source surveillance coupled with dynamic risk modeling is therefore essential for safeguarding national biosecurity.

Nipah virus (NiV) infection represents a highly fatal zoonotic disease that poses a severe threat to global health security. As a World Health Organization (WHO) Research and Development Blueprint priority pathogen, NiV is characterized by an exceptionally high case fatality rate (40%–75%) and frequent spillover events from animal reservoirs to human populations (*1–2*). The extensive global air travel network creates substantial risk for NiV to spread beyond its endemic regions in South and Southeast Asia (*3*). Consequently, quantifying the risk of NiV importation is essential for strengthening national biosecurity frameworks and enhancing early warning capabilities.

As of early 2026, over 700 laboratory-confirmed human cases of NiV have been documented globally, with India emerging as a critical epicenter of recurrent outbreaks (*4*). While initial clusters were primarily localized in Malaysia, Singapore, India, and Bangladesh, genomic and serological surveillance has since identified NiV or NiV-like henipaviruses in approximately 20 countries across the Indo-Pacific and Africa (*2,5*). This geographical expansion closely aligns with the ecological niche of its natural reservoir, fruit bats of the genus *Pteropus* (*6*). Notably, recent outbreaks in South Asia have signaled a concerning shift toward more efficient human-to-human transmission, with secondary attack rates frequently reaching epidemic thresholds (*3*). The intensification of trade and migration between China and these ecologically high-risk zones under the Belt and Road Initiative has significantly elevated the probability of pathogen introduction. This evolving landscape necessitates a high-resolution, spatiotemporal evaluation of NiV importation risks.

Given the rapid spread of emerging infectious diseases (EIDs) in an increasingly interconnected world, the ability to prioritize interventions is critical, particularly when resources and time are constrained. Risk assessment provides a fundamental framework for identifying high-risk areas and characterizing key transmission factors (*7*–*8*). By offering a structured approach to quantify threats, it enables timely and strategic interventions to mitigate the introduction and spread of high-consequence pathogens. Conventional risk assessment methods — ranging from expert-led approaches such as the Delphi technique to complex statistical models — often face a dual challenge: expert-led methods are susceptible to subjective bias, while statistical models are frequently constrained by stringent data requirements and limited data availability (*7*–*8*).

To address these methodological limitations, this study adopts an integrated approach that combines qualitative and quantitative evaluation frameworks. The risk matrix method establishes a robust semi-quantitative structure for categorizing risks according to their likelihood and potential consequences, while the Borda count method provides precise, quantitative ranking of these identified threats. This data-driven integration minimizes subjective weighting bias and enhances discriminatory power, thereby enabling the prioritization of countries even when they fall within identical risk categories. Although this hybrid framework has demonstrated utility in assessing other EIDs — including Ebola, Mpox, and Lassa fever — the specific importation risk of NiV into China remains inadequately characterized. Consequently, this study employs this integrated model to systematically evaluate and rank the risks posed by key NiV-affected countries, with the objective of providing an evidence-based reference for China's early warning systems and strategic preparedness initiatives.

In this study, we categorized and ranked the NiV importation risk across two dimensions — likelihood and consequences — by synthesizing multi-source data including epidemiological profiles, aviation capacity, animal product trade, and geographical proximity.

Epidemiological data — including human NiV cases, deaths, and case fatality rates from five countries (Bangladesh, India, Malaysia, the Philippines, and Singapore) between 1999 and 2026 — were obtained from the WHO Disease Outbreak News, official government websites, and peer-reviewed literature (*4*,*9*–*10*). Risk assessment indicators were synthesized from multiple sources: basic reproductive numbers (R_0) were derived from the WHO and literature; aviation capacity from the Official Aviation Guide (*11*); trade statistics for animals and animal products from the General Administration of Customs of China (GACC) (*12*); and terrestrial border information from geospatial datasets (Table 1).

This study employed a risk matrix to evaluate NiV importation risk into China across two primary dimensions — likelihood and consequences — following WHO Rapid Risk Assessment guidelines (Table 2). Through comprehensive literature review, we identified key indicators for each dimension. Likelihood was assessed using five indicators: cumulative case count, monthly inbound aviation capacity, import value of animals and animal products, terrestrial proximity to China, and outbreak recency (defined as the time interval between the most recent outbreak and 2026). Consequences were determined by two epidemiological parameters: R_0 and cumulative case fatality rate. Risk assessment indicator scores were established through a three-step process. First, we reviewed existing literature on infectious disease importation risk (*7*). Second, we synthesized the epidemiological characteristics of NiV alongside cross-border movement patterns of personnel and cargo between China and the five key countries. Third, we conducted expert consultations to refine the scoring framework. Public health professionals performed the assessment in strict adherence to WHO guidelines (*13*). Classification and scoring criteria were derived from systematic review of multi-source surveillance data to ensure both objectivity and reproducibility. Detailed scoring criteria are presented in Table 3.

The indicator weighting scheme was established based on the epidemiological hierarchy of transmission, assigning the highest priority to the source of infection and primary transmission routes. To align with the WHO risk matrix framework, the Equal Interval Method was employed to stratify the normalized theoretical scores (0–10) linearly into 5 distinct risk levels. (*13*) The formulas for importation likelihood and consequences of NiV are as follows. First, the importation likelihood score was calculated as: the score of the number of cumulative cases × 40% + the score of monthly inbound aviation capacity × 30% +

TABLE 1. Epidemiological profiles and risk assessment indicators for key Nipah virus-affected countries (1999–2026).

Country	Cumulative cases	Cumulative deaths	Case fatality rate (%)	R_0	Monthly inbound aviation capacity (thousand)*†	Trade in animals and animal products (million CNY)†	Terrestrial proximity to China	The time lag between the latest outbreak of Nipah Virus infection and 2026 by country (years)
Bangladesh	348	250	71.84	0.33–0.48	36	56.93	Non-bordering but proximal	0
India	106	74	69.81	~0.33	26	1,252.20	Bordering with natural barriers	0
Malaysia	265	105	39.62	~0	290	1,202.01	Non-adjacent and ocean-isolated	27
Philippines	17	9	52.94	~0	135	163.88	Non-adjacent and ocean-isolated	12
Singapore	11	1	9.09	<0.1	375	34.95	Non-adjacent and ocean-isolated	27

Note: ~ means around.

Abbreviation: CNY=Chinese Yuan; R_0=basic reproductive number.

* data represent total monthly seats capacity for inbound routes to China;

† monthly data; cumulative cases and cumulative case fatality rate (%) of Nipah virus infection were from the year of 1999–2026.

TABLE 2. Risk matrix.

Likelihood	Consequences				
	Minimal	Minor	Moderate	Major	Severe
Almost certain	L	M	H	VH	VH
Highly likely	L	M	H	VH	VH
Likely	L	M	H	H	VH
Unlikely	L	L	M	H	H
Very unlikely	L	L	M	H	H

Note: Actions and response framework (based on WHO guidelines): L (Low risk): Managed according to standard response protocols, routine control programmes, and regulation (e.g., monitoring through routine surveillance systems). M (Moderate risk): Roles and responsibilities for the response must be specified; specific monitoring or control measures are required (e.g., enhanced surveillance). H (High risk): Senior management attention is needed; there may be a need to establish command and control structures; a range of additional control measures will be required, some of which may have significant consequences. VH (Very high risk): Immediate response is required even if the event is reported out of normal working hours; immediate senior management attention is needed (e.g., establishing command structures within hours); the implementation of control measures with serious consequences is highly likely.

the score of monthly importation value of animals and animal products × 10% + the score of terrestrial proximity to China × 10% + the score of the time from the last outbreak to 2026 × 10%. This study then derived the importation likelihood risk score using 5 levels: very unlikely (0–2 points); unlikely (3–4 points); likely (5–6 points); highly likely (7–8 points); and almost certain (9–10 points). The time lag in years between the latest outbreak of NiV and 2026 was calculated by country as 2026 minus the outbreak year. Second, the importation consequences score was calculated as R_0 score plus the cumulative case fatality rate score. Cumulative cases were equal to the total number of cases in countries with NiV from 1999–2026. $Cumulative\ case\ fatality\ rates = \frac{cumulative\ deaths\ from\ 1999\ to\ 2026}{cumulative\ cases\ from\ 1999\ to\ 2026} \times 100\%$ This study classified the final importation consequences risk score into 5 levels: minimal (0–2 points); minor (3–4 points); moderate (5–6 points); major (7–8 points); and severe (9–10 points). Third, according to the importation likelihood and consequences levels in the risk matrix (Table 2), the importation risk of NiV into China was divided into 4 levels (low, moderate, high, and very high), which corresponded to green, yellow, orange, and red zones, respectively. Finally, this study used the Borda count method to rank the NiV importation risk (*7*).

This study used the Borda count method to rank NiV importation risks. First, the Borda points for each importation risk were calculated as the sum of the rank of its importation likelihood and the rank of its consequences risk level (*7*). This study then sorted the Borda points from largest to smallest and assigned corresponding counts of 0, 1, …, N-1. A lower Borda count indicates a greater likelihood of NiV importation to China and potentially more severe consequences. Borda points were calculated using the following

TABLE 3. Risk assessment indicators of importation likelihood, consequences, and corresponding scores.

Assessment indicators	Factors	Classification	Risk score
Importation likelihood	Cumulative cases	≤49	2
		50–499	4
		500–999	6
		1,000–4,999	8
		≥5,000	10
	Monthly inbound aviation capacity (seats)*†	≤49	2
		50–299	4
		300–799	6
		800–1,499	8
		≥1,500	10
	Monthly importation value of animals and animal products (Million CNY)†	≤49	2
		50–499	4
		500–1,999	6
		2,000–4,999	8
		≥5,000	10
	Terrestrial proximity to China	Non-adjacent and ocean-isolated	2
		Non-bordering but proximal	4
		Bordering with natural barriers	6
		Bordering with land ports of entry	8
		Bordering with extensive, porous boundaries	10
	The time lag between the latest outbreak of Nipah virus infection and 2026 by country (years)	≤1	10
		2–3	8
		4–5	6
		6–9	4
		≥10	2
Importation consequences	R_0	≤0.5	2
		0.6–0.9	4
		1–1.4	6
		1.5–2.4	8
		≥2.5	10
	Cumulative case fatality rate (%)	≤9	2
		10–39	4
		40–59	6
		60–79	8
		≥80	10

Abbreviation: CNY=Chinese Yuan; R0=basic reproductive number.

* data represent total monthly seats capacity for inbound routes to China;

† monthly data; cumulative cases and cumulative case fatality rate (%) of Nipah virus infection were from the year of 1999–2026.

formula:

$$b_i = \sum_{k=1}^{m} (N - r_{ik})$$

Where N equals the total number of at-risk countries, this study defined at-risk countries as those with NiV importation risk. Therefore, this study set N as 5. The variable m equals the 2 dimensions of risk assessment. r_{ik} equals the number of countries posing a higher risk than the risk for indicator i under criterion k, and b_i equals the Borda points of assessment indicator i.

This study scored and ranked the risk of NiV importation for 5 countries that experienced outbreaks from 1999 to 2026. It considered global importation likelihood and consequences to derive overall importation risks (Table 4). Using a risk matrix diagram, this study then visualized these total risks, with red, orange, yellow, and green representing very high, high, moderate, and low importation risk, respectively (Figure 1). Its integrated application of the risk matrix and Borda count method demonstrated that China faces a risk of NiV importation. Regarding importation likelihood, India presented the highest risk (score=4.4), while the Philippines presented the lowest (score=2.8). Concerning importation consequences, India and Bangladesh exhibited the highest risk (score=5), whereas Singapore had the lowest (score=2) (Table 4). India and Bangladesh posed a moderate NiV importation risk (Figure 1) due to the highest Borda points of 10 and ranking first. Malaysia, Singapore, and the Philippines presented low importation risks (Figure 1). The Philippines exhibited the lowest Borda points of 4 and ranked fifth (Table 4).

DISCUSSION

This study employs an integrated risk matrix and Borda count approach to quantify the risk of NiV importation into China. By combining structured professional assessment with multi-sectoral indicators — specifically civil aviation and animal trade data — this framework enhances the granularity of risk exposure assessment from personnel mobility and potential fomite transmission. Unlike models that rely exclusively on reported health data, this multi-dimensional analysis offers a practical tool for identifying high-risk monitoring nodes in data-limited scenarios. These rankings provide a reproducible reference for prioritizing high-risk importation sources, thereby enabling more targeted resource allocation and strategic containment measures.

This study determined that India and Bangladesh pose a moderate risk of NiV importation to China, characterized by high consequences despite an "unlikely" likelihood of immediate large-scale introduction. This elevated risk is primarily driven by

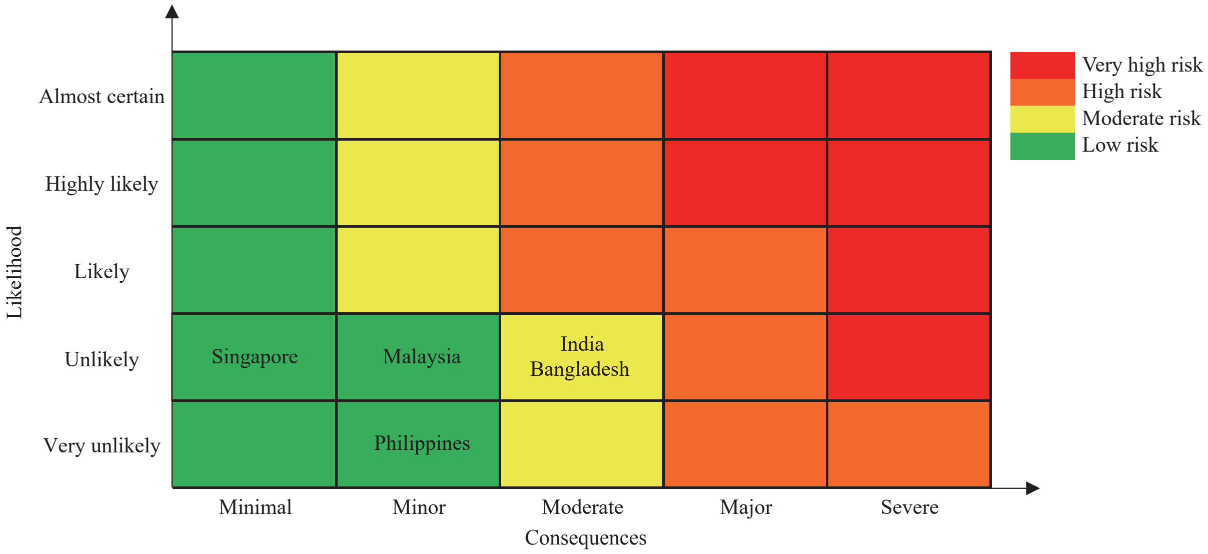

FIGURE 1. Importation risk of Nipah virus infection.

TABLE 4. Importation risks from countries with Nipah virus infection outbreaks to China from 1999–2026.

Country name	Importation likelihood score	Importation consequences score	Risk levels	Borda points	Borda count	Risk sequence of importation
India	4.4	5	M	10	0	1
Bangladesh	4.0	5	M	10	0	1
Malaysia	3.8	3	L	8	2	3
Singapore	3.2	2	L	6	3	4
Philippines	2.8	4	L	4	4	5

Abbreviation: L=low risk; M=moderate risk.

the dominance of the NiV-Bangladesh/India lineage (NiV-B). Compared to the Malaysian genotype (NiV-M), NiV-B demonstrates human-to-human transmissibility and exhibits a significantly higher case fatality rate (40%–75%) (*14–15*). Furthermore, phylogenetic analyses indicate that NiV-B possesses substantial evolutionary potential, raising concerns about its capacity to evolve enhanced transmissibility traits (*15*). This risk stems from a convergence of critical factors: high lethality, respiratory symptoms that facilitate human-to-human transmission, and frequent spillover events in densely populated regions (*1*,*15*). Collectively, these elements underscore a persistent and evolving threat to regional biosecurity. Notably, while the genetic lineages of NiV (e.g., NiV-B and NiV-M) differentially influence human-to-human transmissibility and virulence, they were not treated as standalone variables in the risk matrix to avoid multicollinearity. Instead, the epidemiological impacts of distinct lineages were inherently quantified through the case fatality rate and R_0 indicators within the consequences dimension. Consequently, countries predominantly affected by the highly virulent NiV-B lineage received higher consequence scores, ensuring that the biological threat of the specific viral strain was objectively integrated into the final risk ranking.

Transmission of NiV-B is markedly amplified in confined settings, particularly healthcare facilities. The 2018 Kerala outbreak demonstrated that index cases with persistent respiratory distress triggered superspreading events, infecting over 10 contacts through droplet transmission — a pattern that typically intensifies during the terminal phase of infection (*16*). The January 2026 outbreak in West Bengal exhibited a similar nosocomial transmission pattern within Kolkata (*3*). These recurring events underscore the persistent risk of viral amplification in healthcare settings, especially in dense urban environments where the virus can exploit high population density to facilitate broader community spread.

Beyond the immediate threat of nosocomial amplification, the endemic persistence of NiV in South Asia stems from a specific socio-ecological nexus that drives marked seasonality from December through May. This epidemic window coincides precisely with the traditional harvesting season for raw date palm sap (*1*,*14–15*). Overnight exposure of open collection containers attracts foraging by *Pteropus medius* fruit bats, the natural reservoir, resulting in sap contamination through infected saliva or excreta. This unique spillover pathway enables the virus to breach species barriers and seed recurrent human infections (*15*). Although local surveillance capacity has improved, the underlying threat of cross-border transmission persists, driven by extreme population density and the clinical difficulty of differentiating NiV from other endemic febrile illnesses in the region.

The confirmed NiV case in the Rajshahi Division of Bangladesh in early February 2026 provides empirical validation of the risk factors identified in this study (*17*). The case occurred during the characteristic low-temperature, dry-winter transmission window and within the high-risk “Nipah Belt,” where human settlements overlap with fruit bat habitats — consistent with the temporal and spatial risk patterns identified in our analysis. The fatal outcome following exposure through raw date palm sap consumption in a high-density rural setting further aligns with the behavioral and demographic drivers we highlighted. The rapid clinical progression and 100% case fatality rate underscore both the high virulence and predominantly sporadic transmission dynamics of NiV. While such extreme virulence may constrain sustained human-to-human transmission and reduce the probability of frequent cross-border spread through large-scale outbreaks, it indicates that even a single imported case could present a substantial public health challenge. This low-frequency, high-consequence risk profile justifies the designation of Bangladesh as a moderate, rather than low, importation risk for China.

Furthermore, the public health capacities of endemic countries substantially influence the magnitude of NiV outbreaks and the level of transnational transmission risk. Although India features relatively robust rapid response and diagnostic networks, delayed early clinical recognition frequently triggers severe nosocomial amplification (*3*,*16*). Conversely, in Bangladesh, spillover events are mainly dispersed across remote rural areas, where surveillance blind spots and inadequate differential diagnostic capability often result in unnoticed early community transmission (*4*,*17*). Collectively, these systemic vulnerabilities may create a critical time window for the unmonitored dissemination of the pathogen. Consequently, despite overall improvements in local epidemic containment, such public health gaps sustain the baseline probability of stochastic exportation by individuals in the incubation period. These factors further underscore the necessity for China to maintain continuous border surveillance, quarantine measures, and risk assessments.

Despite these combined biological threats and systemic public health vulnerabilities, the likelihood of importation into China remains Unlikely. The Himalayan massif functions as a formidable natural buffer, while the current volume of direct aviation flux between the affected South Asian regions and Chinese ports of entry remains relatively low. Crucially, this residual risk is effectively mitigated by China's proactive biosecurity framework. In 2021, the China CDC issued technical guidelines that established standardized molecular assays and provided a framework for the stockpiling of emergency diagnostic kits. This was followed in 2024 by the designation of NiV as a priority target for frontier health and quarantine (*18–19*). Recently, during the January 2026 outbreak, the GACC and China CDC have initiated intensified measures, including mandatory border screenings, the decentralization of laboratory identification to provincial centers, and the clinical evaluation of domestic antiviral candidates (*20*). These measures establish a robust defensive shield against stochastic importation. However, in a globalized context, the potential for stochastic entry via highly mobile populations remains a persistent threat.

The quantitative results may provide a reference for optimizing control strategies for customs and public health authorities. For travelers from moderate-risk regions, targeted surveillance combining symptom screening with travel history verification is advised, particularly during the NiV infection outbreak season (Winter/Spring). Simultaneously, risk-based inspection should prioritize high-risk vectors, such as fresh fruits in commercial trade and unregulated biological products, to intercept potential viral importation. Furthermore, given NiV's exceptional lethality, strengthened preparedness — including enhanced diagnostic and clinical response capacity — is essential to mitigate low-likelihood, high-consequence risks.

This study has several limitations that warrant caution when interpreting the results. First, this assessment was conducted as a rapid risk assessment and therefore did not include a multi-expert elicitation process (e.g., Delphi panels). Although scoring was guided by predefined evidence-based criteria and WHO Rapid Risk Assessment guidance, some uncertainty may remain in cut-off selection and weighting. Second, as an ordinal measure, the Borda count captures the relative positioning of risks but does not quantify the absolute magnitude of differences between specific rankings. Third, the risk matrix does not explicitly incorporate dynamic biological data of *Pteropus* bats, including population density, migratory patterns, or seasonal viral shedding, which may affect spillover dynamics. In addition, while the broad seasonality of NiV outbreaks is captured, the model does not fully parameterize the influence of climatic fluctuations on host spatial distribution, potentially overlooking localized high-risk areas. Fourth, the assessment focused on countries with historically confirmed human cases, which may omit potential de novo introductions from other regions within the reservoir range. Lastly, differences in surveillance sensitivity and diagnostic capacity across countries could lead to underestimation of risk, particularly in resource-limited settings. Despite these limitations, prioritizing established endemic zones remains a pragmatic strategy for current resource allocation. Future frameworks should integrate multi-source ecological niche modeling and health-system data to enhance the precision of risk assessments.

Conflicts of interest: No conflicts of interest.

Funding: Supported by the Beijing Natural Science Foundation (grant number 7254473), and the Prevention and Control of Emerging and Major Infectious Diseases-National Science and Technology Major Project (grant number 2025ZD01901600).

doi: 10.46234/ccdcw2026.035

Corresponding author: Qiwen Zheng, zhengqw@big.ac.cn.

---

[1] China National Center for Bioinformation, Beijing, China; [2] Beijing Institute of Genomics, Chinese Academy of Sciences, Beijing, China.

Submitted: February 06, 2026
Accepted: February 18, 2026
Issued: February 20, 2026

REFERENCES

1. Tan FH, Sukri A, Idris N, Ong KC, Schee JP, Tan CT, et al. A systematic review on Nipah virus: global molecular epidemiology and medical countermeasures development. Virus Evol 2024;10(1):veae048. https://doi.org/10.1093/ve/veae048.
2. WHO. WHO South-East Asia regional strategy for the prevention and control of Nipah virus infection 2023-2030. 2023. https://www.who.int/publications/i/item/9789290210849. [2026-1-30].
3. WHO. Nipah virus infection - India. 2026. https://www.who.int/emergencies/disease-outbreak-news/item/2026-DON593. [2026-1-30].
4. WHO. Disease outbreak news (DONs). 2026. https://www.who.int/emergencies/disease-outbreak-news. [2026-1-30].
5. Li HZ, Kim JYV, Pickering BS. Henipavirus zoonosis: outbreaks, animal hosts and potential new emergence. Front Microbiol 2023;14:1167085. https://doi.org/10.3389/fmicb.2023.1167085.
6. Sun YQ, Zhang YY, Liu MC, Chen JJ, Li TT, Liu YN, et al. Mapping the distribution of Nipah virus infections: a geospatial modelling analysis. Lancet Planet Health 2024;8(7):e463 – 75. https://doi.org/10.1016/S2542-5196(24)00119-0.

7. Shang WJ, Wu Y, Liu J, Liang WN, Liu M. Application of an integrated risk matrix and the borda count method on lassa fever in assessing the importation risk of EID - 9 African countries, 1996-2023. China CDC Wkly 2024;6(44):1152 – 8. https://doi.org/10.46234/ccdcw2024.234.
8. China CDC. Technical program for public health risk assessment of emergencies (trial). 2017. https://www.chinacdc.cn/jkyj/tfggws/jswj1/201708/t20170810_301463.html. [2026-1-30]. (In Chinese).
9. Veggalam S, Ca J, Balaji O, Madhu MT, Hussain MH, Shraddha H, et al. Nipah virus outbreaks in India: a comprehensive update. Cureus 2025;17(9):e92420. https://doi.org/10.7759/cureus.92420.
10. Satter SM, Aquib WR, Sultana S, Sharif AR, Nazneen A, Alam MR, et al. Tackling a global epidemic threat: Nipah surveillance in Bangladesh, 2006-2021. PLoS Negl Trop Dis 2023;17(9):e0011617. https://doi.org/10.1371/journal.pntd.0011617.
11. Official Aviation Guide. Airline capacity data. 2026. https://www.oag.cn/flight-data-seats. [2026-1-30]. (In Chinese).
12. China General Administration of Customs. Online query platform for customs statistics. 2026. http://stats.customs.gov.cn/. [2026-1-29]. (In Chinese).
13. WHO. WHO rapid risk assessment guidance v.2.1. 2025. https://www.who.int/publications/m/item/who-rapid-risk-assessment-guidance-v.2.1. [2026-2-8].
14. Hantabal J, Salguero FJ, Carroll MW. Current knowledge on the host-pathogen interactions of henipaviruses and novel platforms to enable further characterisation. eBioMedicine 2026;123:106110. https://doi.org/10.1016/j.ebiom.2025.106110.
15. Madhukalya R, Yadav U, Parray HA, Raj N, Lupitha SS, Kumar V, et al. Nipah virus: pathogenesis, genome, diagnosis, and treatment. Appl Microbiol Biotechnol 2025;109(1):158. https://doi.org/10.1007/s00253-025-13474-6.
16. Arunkumar G, Chandni R, Mourya DT, Singh SK, Sadanandan R, Sudan P, et al. Outbreak investigation of Nipah virus disease in Kerala, India, 2018. J Infect Dis 2019;219(12):1867 – 78. https://doi.org/10.1093/infdis/jiy612.
17. WHO. Disease outbreak news; Nipah virus infection - Bangladesh. 2026.https://www.who.int/emergencies/disease-outbreak-news/item/2026-DON594. [2026-2-8].
18. China CDC. Notice on issuing the technical guidelines for prevention and control of Nipah virus disease. 2021. https://sph.sustech.edu.cn/uploads/file/20260127/1769505275325174.pdf. [2026-1-30]. (In Chinese).
19. China General Administration of Customs. Announcement on publishing the list of monitored infectious diseases (joint announcement No. 3 of 2024). 2024. http://www.customs.gov.cn/customs/2024-12/30/article_2025121223523568389.html. [2026-1-30]. (In Chinese).
20. China General Administration of Customs. Health advisory for overseas travel: scientific prevention and control of Nipah virus disease. 2026. http://wss.customs.gov.cn/wss/2026-01/27/article_2026012710135454019.html. [2026-1-30]. (In Chinese).

Preplanned Studies

Retrospective Analysis of the Molecular Links Among Clustered Cases of *Acinetobacter baumannii* Nosocomial Infections Occurring in Different Years within the ICU — Jiangsu Province, China, 2016–2021

Xiaosong Wu[1,&]; Jingjing Fan[2,&]; Liye Huang[3,&]; Yiping Mao[4]; Yang Wang[5]; Yiming Shen[2]; Huimin Qian[2];
Lumei Wang[3]; Xiaobin Wang[4]; Tingting Ni[3]; Li Liang[3]; Shanshan Ye[1]; Chenxue Zhu[1];
Jun Bi[3]; Jianming Wang[1,#]; Yan Xu[1,2,6,#]

Summary

What is already known about this topic?

Carbapenem-resistant *Acinetobacter baumannii* (CRAB) is a well-established cause of difficult-to-treat nosocomial infections, particularly in intensive care units (ICUs). This strain is known for its ability to persist in hospital environments, leading to outbreaks.

What is added by this report?

This retrospective study analyzed five separate CRAB nosocomial infection clusters that occurred in 2016, 2019, and 2021. This revealed the molecular epidemiological links between cases and environmental samples across different years, suggesting the potential for ongoing environmental transmission. Following intensive terminal disinfection, no homologous pathogens have been detected since 2021.

What are the implications for public health practice?

The potential risk of environmental transmission suggests that the current bedside isolation strategies may have deficiencies. Given that the prevailing ICU multibedroom configuration remains unchanged, additional effective disinfection methods must be developed urgently. These techniques should specifically target high-touch irregular surfaces to disrupt persistent CRAB transmission.

ABSTRACT

Introduction: To investigate the molecular epidemiological links among clustered cases of carbapenem-resistant *Acinetobacter baumannii* (CRAB) nosocomial infections occurring in different years within an intensive care unit (ICU) in Jiangsu Province, China and identify gaps in infection control in multibed ICU settings.

Methods: A retrospective study was conducted on five clusters of CRAB infections in 2016, 2019, and 2021. Twenty clinical and forty environmental *A. baumannii* isolates were analyzed using pulsed-field gel electrophoresis (PFGE) for molecular typing, and antimicrobial susceptibility testing for resistance profiling.

Results: PFGE revealed high genetic similarity (>90%) among clinical and environmental isolates from 2016, 2019, and 2021, indicating the persistent environmental transmission of CRAB over multiple years. All patient-derived strains were CRAB strains. No homologous strains were detected after thorough disinfection of the terminals in 2021.

Conclusions: CRAB demonstrated remarkable environmental persistence in ICUs, suggesting limitations in current disinfection practices. Enhanced disinfection strategies targeting high-touch complex surfaces are necessary to interrupt CRAB transmission and reduce nosocomial outbreaks.

Acinetobacter baumannii is a conditionally pathogenic gram-negative bacterium that has emerged as a major pathogen causing hospital infection outbreaks because of its ability to adapt to various environmental conditions. As a critical multidrug-resistant pathogen in nosocomial infections, *A. baumannii* has accounted for more than 10% of all gram-negative hospital infections in intensive care units (ICUs) in Europe and the United States over the last 10 years, and this proportion continues to rise (*1–2*). The mortality rate associated with nosocomial outbreaks, which were mainly reported from ICUs (104 in ICU/150 total), caused by *A. baumannii* is approximately 48% multi-drugresistant and 42.5%

non-multidrug resistant (*3*). Moreover, the World Health Organization (WHO) has classified Carbapenem-resistant *Acinetobacter baumannii* (CRAB) as a critical group of bacteria that poses the most severe threat to human health (*4*).

In China, this situation is of equal concern and cannot be overlooked. The 2023 China Bacterial Drug Resistance Surveillance revealed that *A. baumannii* accounted for 87.6% of Acinetobacter spp. The resistance rates of these strains to all antibiotics except polymyxin and tigecycline exceeded 48%. The resistance rates of *A. baumannii* to meropenem and imipenem were 73.7% and 73.4%, respectively, ranking fourth among the top 20 most important clinical isolates (*5*). Owing to its pan-drug resistance, *A. baumannii* has become a formidable challenge for infection control in intensive care wards and a notable cause of death among patients with severe infections.

In a single ward with abundant hospital resources, isolation and terminal disinfection measures have effectively controlled drug-resistant bacteria, including *A. baumannii* (*6*). However, ICUs are rarely designed as single-room ward models. Instead, they generally have multibed, large-room layouts. Patients in ICUs have extended stays and are not easily moved. Once hospital infections occur, isolation becomes ineffective, and disinfection serves as the sole measure to cut off transmission routes. This study aimed to explore the molecular link between multiple clusters of CRAB nosocomial infections in different years and to identify gaps in the current disinfection protocols for multibed ICUs in a hospital in Jiangsu Province, China.

A tertiary hospital in Jiangsu Province with approximately 4,000 beds was selected for this study. The emergency ICU consisted of 8 wards with 25 beds. *A. baumannii* strains were obtained from different aggregated cases in the emergency ICU during 2016–2021 from different aggregated cases (According to the guidelines for the control of healthcare-associated infection outbreaks WS/T 524-2016, the occurrence of 3 cases of hospital-acquired infections with the same pathogenic microorganism was regarded as an aggregated case) and the related ICU circumstances. Related pathogen surveillance was conducted from 2021 to 2024, following thorough terminal disinfection. Samples were collected from the sputum, blood, and wounds (Figure 1).

Environmental samples were collected by converting the high-contact surfaces of the ICU (bed rails, device controls/screens, charts, and call buttons) and general wards (door handles, carts, faucets, and sinks), nurses' stations (staff white coats, work surfaces, faucets/sinks, and drawer handles/phones), and dispensing and cleaning rooms (countertops, carts, faucets/sinks, door handles, and cleaning tools).

Bacterial isolates were initially purified on chromogenic medium plates. Species identification was performed using matrix-assisted laser desorption ionization time-of-flight mass spectrometry, calibrated with *Salmonella* H9812, and the results were analyzed using the Myla system. Antimicrobial susceptibility testing (AST) of *A. baumannii* utilized the VITEK2 system with GN AST-09 cards. Molecular typing of isolates was conducted via pulsed-field gel electrophoresis (PFGE) using the CHEF MAPPER™ system (BIO-RAD); DNA was digested by the *ApaI* restriction enzyme. The PFGE process was carried out at a voltage gradient of 6.0 V/cm, an angle of 120°, a temperature of 14 ℃, with pulse time ranging from 5–20 s, and lasted 18.5 h. PFGE gel images were analyzed using BioNumerics software. *A. baumannii* strains exhibiting more than 90% similarity based on Dice coefficients were classified as related strains.

A total of 5 aggregated clusters involving 19 patients were identified in 2016 (1st cluster, 3 cases), 2019 (2nd cluster, 4 cases; 3rd cluster, 5 cases; 4th cluster, 2 cases), and 2021 (5th cluster, 2 cases). From these clusters, 20 *A. baumannii* strains were isolated (2 strains were isolated from the patient's exudate and peritoneal drainage fluid, respectively) (Supplementary Table S1, available at https://weekly.chinacdc.cn/). In addition, 40 *A. baumannii* strains were isolated from the environmental samples (Supplementary Table S2, available at https://weekly.chinacdc.cn/). Among the 19 patients, 10 were co-infected with other pathogens, specifically *Klebsiella*.

The AST results for all isolates are presented in Supplementary Table S2. Among the 60 *A. baumannii* strains, 86.7% (52/60) were CRAB, including all 20 strains isolated from patients. Among the 52 strains exhibiting resistance to imipenem, 40 were resistant to meropenem and were recognized as CRAB.

PFGE was performed on 60 isolates, including 20 clinical and 40 environmental isolates. The 60 isolates were divided into 9 groups using a similarity cutoff of 90% (Figure 1). The largest group, A, comprised 29 isolates, including 10 from 9 patients (1st, 2nd, and 5th cluster patients in 2016, 2019, and 2021, respectively) and 19 from the relevant environment. The second largest group D had 16 isolates (3rd and 4th clusters in March and October-November in 2019, respectively) and the 9 related environmental isolates

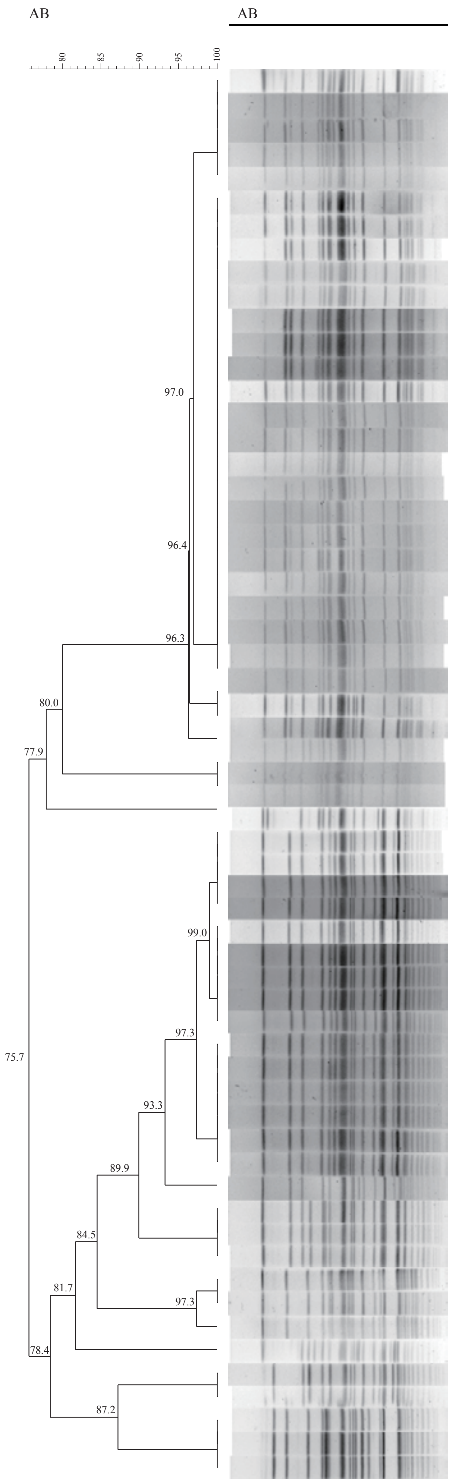

Study ID	Bed no. Location/Source	Type
XZ210910ABP001	23 sputum	A
XZ160623ABP012	13 sputum	A
XZ160606ABP018	14 exudate	A
XZ160601ABE010*	18 computer mouse	A
XZ160601ABE011*	18 computer keyboard	A
XZ191010ABP001	9 sputum	A
XZ191012ABP003	6 sputum	A
XZ191012ABP005	18 sputum	A
XZ190318ABE015	23 glucometer cartridge	A
XZ190318ABE016	24 bed rails	A
XZ190319ABE003	5 surface of syringe pump	A
XZ190319ABE004	17 ventilator valve	A
XZ190319ABE007	19 writing trolley table top	A
XZ210916ABP003	5 sputum	A
XZ160601ABE001*	13 treatment table handle	A
XZ160601ABE003*	23 bed rails	A
XZ160601ABE004*	11 ventilator buttons	A
XZ160704ABE014*	15 ventilator buttons	A
XZ160601ABE005	2 therapeutic trolley table	A
XZ160704ABE015	8 bed rails	A
XZ160606ABP013	14 abdominal drainage	A
XZ160601ABE006	23 ventilator air heater	A
XZ160601ABP007	8 sputum	A
XZ160601ABE008*	11 therapeutic trolley table	A
XZ160704ABE016	8 writing desk	A
XZ160601ABE009*	13 ventilator button	A
XZ191012ABP002	8 blood	A
XZ190319ABE013	17 bed rails	A
XZ160704ABE017	8 cardiac monitor botton	A
XZ160601ABE002	23 ventilator connection	B
XZ160704ABE013	8 infusion pump	B
XZ210910ABP002	18 sputum	C
XZ191118ABP008	12 sputum	D
XZ191009ABP009	6 sputum	D
XZ190318ABP018	5 sputum	D
XZ190323ABP026	2 sputum	D
XZ191021ABE005	White coats	D
XZ190318ABP019	11 sputum	D
XZ190318ABP020	1 sputum	D
XZ190318ABP021	4 sputum	D
XZ190318ABE002	5 bed rails	D
XZ190319ABE005	17 syringe pump	D
XZ190319ABE006	18 bed handle buttons	D
XZ190318ABE008	16 bed rails	D
XZ190321ABE009	21 writing trolley top	D
XZ190318ABE011	14 PDA surface	D
XZ190318ABE012	14 bed rails	D
XZ160704ABE019	15 cardiac monitor	D
XZ210915ABE001	6 bedside table	E
XZ210915ABE002	6 medical record folder	E
XZ210915ABE018	15 headboard	E
XZ191021ABE004	tap switch and spout	F
XZ191021ABE010	nurse 3's hand (ungloved)	F
XZ191021ABE001	18 headboard	F
XZ210913ABP004	25 sputum	G
XZ210915ABE004	6 ventilator connection	H
XZ210909ABP005	22 sputum	H
XZ191021ABE006	drawer handles	I
XZ191021ABE007	door handles	I
XZ191021ABE009	nurse 1's hand (ungloved)	I

FIGURE 1. PFGE dendrogram of *A. baumannii* aggregated case groups by bed number, location, and source.

Note: 60 isolates (20 clinical and 40 environmental isolates) were included. The cluster analysis dendrogram is a molecular analysis performed by BioNumerics software to classify different *A. baumannii* strains based on band similarity, with a similarity value greater than 90% indicating the same origin. Study ID refers to the research identification numbers assigned in this study to *A. baumannii* strains isolated from patients or the environment. The Study IDs with an asterisk denote non-carbapenem *Acinetobacter baumannii* isolates. Bed No. location/source indicates the bed number and the type of patient specimen/environmental location from which the strain was isolated. Type denotes clusters identified by the software as strains of the same origin.

Abbreviation: AB=*A. baumannii*=*Acinetobacter baumannii*; PFGE=pulsed-field gel electrophoresis; ID=Identity Document.

(notably including a sample from 2016).

As confirmed by PFGE, the aggregated cases in June 2016 (3 cases) were identified as the same type of CRAB infection. Notably, 4 patients in 2019 (XZ191010ABP001, XZ191012ABP003, XZ191012ABP002, and XZ191012ABP005) and 2 patients in 2021 (XZ210910ABP001 and XZ210916ABP003) were also infected with the same type of CRAB as in 2016 (Figure 1). With regard to the locations of the patient and environmental samples, in 2016, the aggregated cases came from 2 multibed rooms (bed 8 in room 2 and beds 13 and 14 in room 3). The contaminated environmental area included the adjacent multibed room (*4*), the more distant double room (*7*), and the multibed room where the cases were located. The collected environmental area included 7 beds and 13 locations. In 2019, the aggregated cases were from 3 multibed rooms (bed 6 in room 1; beds 8 and 9 in room 2; and bed 18 in room 4). The contaminated environmental areas included the more distant double room 7 and multibed rooms where the cases were located. The collection area consisted of 5 beds and 6 locations. In 2021, the aggregated cases came from 2 multibed rooms (bed 5 in room 1 and bed 23 in room 7), and the environmental areas in these rooms were not contaminated (Figure 2A).

The second largest group of aggregated cases (group D), identified by PFGE, consisted of 5 cases in March 2019 and 2 cases from October to November 2019. These cases are homologous to those of the 2016 single-strain environmental samples. In March 2019, the cases came from beds 1, 2, 4, and 5 in room 1 and bed 11 in room 2, situated in 2 adjacent multiplexes (rooms 1 and 2). The contaminated environmental areas extended beyond the rooms where the patients stayed, encompassing adjacent multibed rooms 3 and 4 and a single room 5. Environmental samples were collected from 6 locations in the study area. During October-November, the aggregated cases came from bed 6 in room 1 and bed 12 in room 2. The contaminated environmental areas included nurse stations (Figure 2B).

DISCUSSION

In this retrospective study, molecular biology methods were successfully employed to trace multiple cases of clustered hospital-acquired infections in 2016 and beyond. These infections originated from both patients and the environment. Given that the study setting was an acute-care ICU, the hospital did not screen every admitted patient for multidrug-resistant bacteria and prior pathogen preservation from this ICU was not available. Consequently, determining whether the initial infections in 2016 were community-acquired or hospital-acquired/colonized was difficult. Using molecular biology analyses, subsequent cases (XZ160620ABP012 in 2016, 4 cases in 2019, and 2 cases in 2021) were judged to be molecular epidemiology-related and may be of the same origin. This retrospective analysis found that CRAB infections in ICUs in China shared similarities with the colonization and infection of VIM-producing *Pseudomonas aeruginosa* and NDM-producing *Enterobacteriaceae* in adults admitted to the ICU of a tertiary care hospital in Belgium between 2018 and 2022 (*7*).

PFGE confirmed that the aggregated cases in March 2019 (5 cases) and October–November 2019 (2 cases) were possibly caused by the same CRAB strain. According to the analysis of the sample collection time, the source of these 2 clustered cases was likely an environmental pathogen (XZ160704ABE019) collected from a 15-bed cardiac monitor in 2016. This study hypothesized that the buttons of cardiac monitors are an environmental reservoir of *A. baumannii*, along with the ventilators (7 samples) and syringe pumps (3 samples) used in this study. Such equipment with buttons is difficult to disinfect (*8*) and can facilitate the spread of infection through contact transmission, which can lead to associated transmission when healthcare workers fail to change gloves or perform hand hygiene after touching the equipment.

The transmission routes of the aggregated cases were analyzed. Although the study spanned a long time, this study was able to initially rule out the sharing of medical equipment as a possible transmission route by determining the source of the environmental samples. In contrast to previously published studies (*9*), *A. baumannii* environmental isolates were collected from only a few shared medical devices. A possible reason for this is that this study was conducted in the ICU, which generally has better-equipped facilities than the average department and does not require multiple patients to share medical devices. This study found that the only possibility for sharing was in the case of treatment carts, which are mobile medical devices (Figure 2).

A. baumannii bloodstream infections pose a serious risk to human health due to their high mortality rates (*10*). In the present study, infection was detected in only one blood sample (Supplementary Table S2).

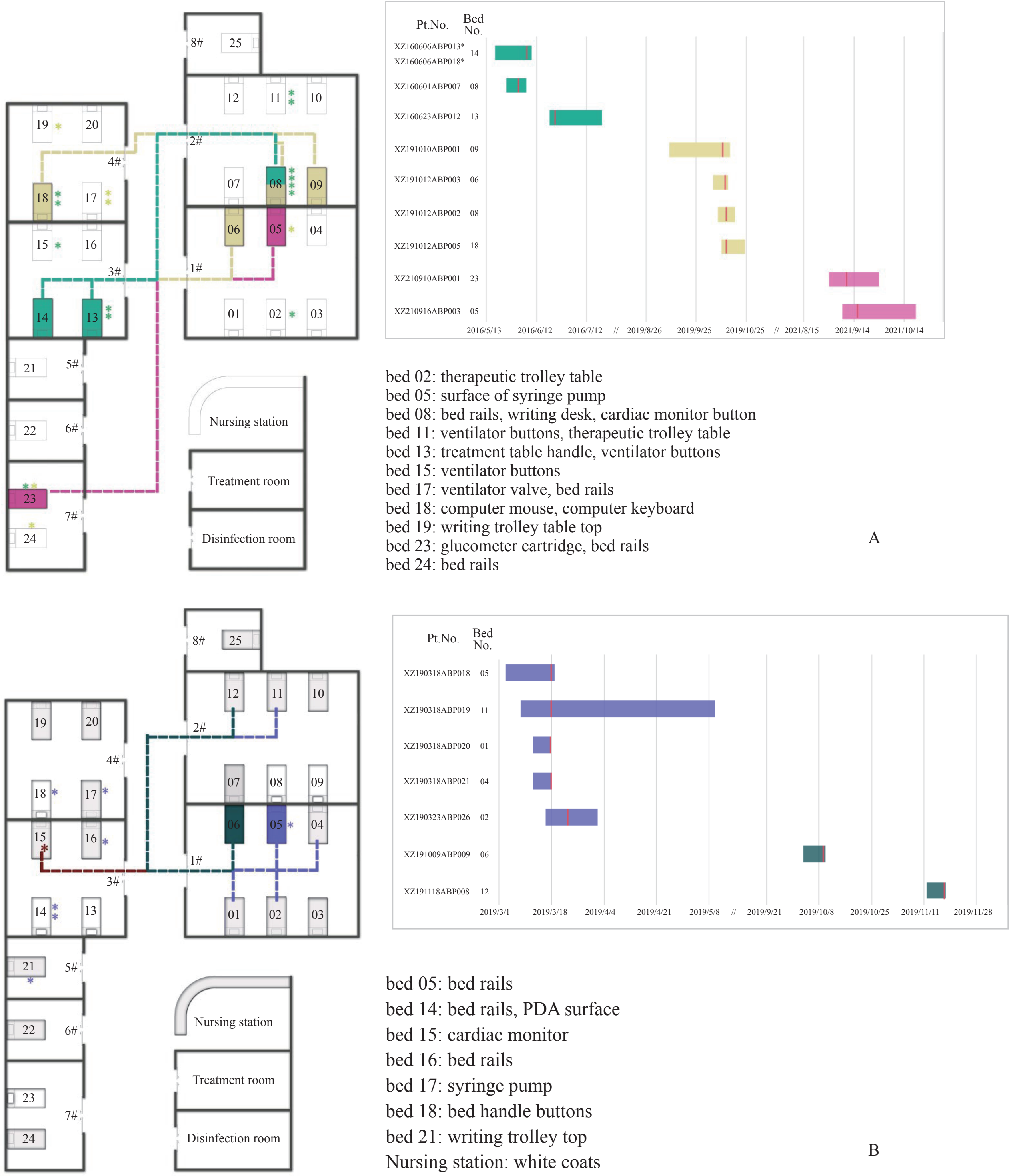

bed 02: therapeutic trolley table
bed 05: surface of syringe pump
bed 08: bed rails, writing desk, cardiac monitor button
bed 11: ventilator buttons, therapeutic trolley table
bed 13: treatment table handle, ventilator buttons
bed 15: ventilator buttons
bed 17: ventilator valve, bed rails
bed 18: computer mouse, computer keyboard
bed 19: writing trolley table top
bed 23: glucometer cartridge, bed rails
bed 24: bed rails

bed 05: bed rails
bed 14: bed rails, PDA surface
bed 15: cardiac monitor
bed 16: bed rails
bed 17: syringe pump
bed 18: bed handle buttons
bed 21: writing trolley top
Nursing station: white coats

FIGURE 2. Summary of environmental positive samples, bed sites of HAI patients, and timeline of aggregated cases in the emergency ICU. (A) The 2016-2019-2021 aggregated cases. Light green, yellow, and magenta represent all samples collected in 2016, 2019, and 2021, respectively; (B) The 2016–2019 (March, Oct–Nov) aggregated cases.

Note: For B, brown, purple, and dark green represent environmental samples collected in 2016, and all samples collected in 2019 and 2021, respectively. All environmental sample collection locations are marked with asterisks on the map, using the same color as the bed positions of clinical cases at the same time, with textual annotations beside the map. Dashed lines represent molecular homology between different clinical cases. The sample collection times of clinical cases are indicated with red vertical lines on the timeline.

Abbreviation: HAI=healthcare-associated Infection; ICU=intensive care unit.

This finding is consistent with that reported by Kong et al. (*11*), who detected infections mainly in respiratory samples. This phenomenon may be related to the high number of mechanical ventilations in ICUs, which is a risk factor for hospital-acquired infections.

Drug sensitivity analysis revealed that all patient specimens were classified as CRAB. Physicians tend to use high-dose ampicillin-sulbactam to treat CRAB infections (*12*). Of the 20 patient samples, 1 (XZ160623ABP012) was resistant to ampicillin, sulbactam, and imipenem. This may lead to difficulties in treatment. However, 32 environmental samples were resistant to both antibiotics, which is another cause for concern. A strain of *A. baumannii* resistant to polymyxin B, imipenem, and meropenem was collected by a nurse. Polymyxins are effective treatments for CRAB (*13*). Bacteria that demonstrate simultaneous resistance to these drugs represent a major obstacle to treatment in the ICU. However, this strain was not detected in the aggregated cases.

In 2016, this study's authors implemented local disinfection measures in the ICU when they identified a short period of aggregated *A. baumannii* infection. No hospital-acquired infections with the same *A. baumannii* strain were recorded during the subsequent period. However, the retrospective discovery of molecularly linked cases in 2019 and 2021 suggests the presence of unidentified environmental reservoirs. Pathogenic microorganisms may still be present in 50% of patients after routine disinfection (*14*). Based on this evidence, the ICU transferred patients temporarily and instituted comprehensive terminal disinfection; no reappearance of relevant strains has been detected since then.

In conclusion, the data strongly imply that CRAB, which is responsible for aggregated cases of infections in ICUs, exhibits remarkable environmental persistence. This study observed that clustered cases occurring in different years over a five-year period may have close molecular epidemiological connections, suggesting that CRAB may pose a potential ongoing risk and could be one of the causes contributing to the occurrence of clustered infections in the ICU. Developing and implementing advanced disinfection techniques (such as vaporized or aerosolized hydrogen peroxide disinfection and the use of antimicrobial surface materials) and protocols tailored specifically to ICU settings are imperative for effectively mitigating CRAB transmission and reducing the incidence of hospital-acquired infections and outbreaks. Improved disinfection measures should target the unique characteristics of CRAB and the ICU environment, interrupt its transmission routes, and safeguard patient health.

This study has some limitations. Due to financial and human resource constraints, it did not follow up or analyze every case of hospital-acquired infection. Patient and environmental samples were collected only when aggregated cases were found in the hospitals. Therefore, the presence of individual cases among the aggregated cases was unclear. This study can only surmise from the molecular correlation that the subsequent aggregated cases might be from the aggregated cases and environmental samples collected in 2016. A clearer molecular epidemiological chain could be established with more comprehensive case tracking. However, the impact of this limitation is constrained, as the conclusions of this study are well supported by the molecular data from the aggregated cases that were collected.

Conflicts of interest: No conflicts of interest.

Ethical statements: Approved by Clinical Research and Ethics Committee of the tertiary hospital (approval no. XYFY2022-KL027-01).

Acknowledgements: The CDC sampling team and hospital staff who helped with data collection and supported our study.

Funding: Supported by the National Natural Science Foundation of China (82473693), Jiangsu Provincial Commission of Health (K2019009, LGY2019074), and Jiangsu Provincial Medical Key Laboratory of Pathogenic Microbiology in Emerging Major Infectious Diseases.

doi: 10.46234/ccdcw2026.034

[#] Corresponding authors: Yan Xu, xuyan@jscdc.cn; Jianming Wang, jmwang@njmu.edu.cn.

---

[1] Department of Epidemiology, Key Laboratory of Public Health Safety and Emergency Prevention and Control Technology of Higher Education Institutions in Jiangsu Province, Center for Global Health, School of Public Health, Nanjing Medical University, Nanjing City, Jiangsu Province, China; [2] Jiangsu Provincial Center for Disease Control and Prevention, Nanjing City, Jiangsu Province, China; [3] Xuzhou Center for Disease Control and Prevention, Xuzhou City, Jiangsu Province, China; [4] Affiliated Hospital of Xuzhou Medical University, Xuzhou City, Jiangsu Province, China; [5] Suzhou Center for Disease Control and Prevention, Suzhou City, Jiangsu Province, China; [6] National Health Committee Key Laboratory of Enteric Pathogenic Microbiology, Nanjing City, Jiangsu Province, China.

[&] Joint first authors.

Submitted: October 10, 2025
Accepted: January 06, 2026
Issued: February 20, 2026

REFERENCES

1. European Centre for Disease Prevention and Control. Antimicrobial resistance surveillance in Europe: annual report of the European antimicrobial resistance surveillance network (EARS-Net). 2014. https://www.ecdc.europa.eu/sites/default/files/media/en/publications/Publications/antimicrobial-resistance-europe-2014.pdf. [2015-11-16].
2. CDC. Antibiotic resistance threats in the United States, 2013. 2013. https://www.cdc.gov/antimicrobial-resistance/media/pdfs/ar-threats-2013-508.pdf.[2013-04-23].
3. Wieland K, Chhatwal P, Vonberg RP. Nosocomial outbreaks caused by *Acinetobacter baumannii* and *Pseudomonas aeruginosa*: results of a systematic review. Am J Infect Control 2018;46(6):643 – 8. https://doi.org/10.1016/j.ajic.2017.12.014.
4. WHO. WHO Bacterial Priority Pathogens List, 2024: bacterial pathogens of public health importance to guide research, development and strategies to prevent and control antimicrobial resistance. 2024. https://www.who.int/publications/i/item/9789240093461.[2024-05-17].
5. China Antimicrobial Resistance Surveillance System. National bacterial drug resistance surveillance report 2023 (brief version). 2024. https://www.carss.cn/Report/Details?aId=978. (In Chinese). [2024-11-28].
6. Anderson DJ, Chen LF, Weber DJ, Moehring RW, Lewis SS, Triplett PF, et al. Enhanced terminal room disinfection and acquisition and infection caused by multidrug-resistant organisms and *Clostridium difficile* (the Benefits of Enhanced Terminal Room Disinfection study): a cluster-randomised, multicentre, crossover study. Lancet 2017;389(10071):805 – 14. https://doi.org/10.1016/S0140-6736(16)31588-4.
7. Anantharajah A, Goormaghtigh F, Nguvuyla Mantu E, Güler B, Bearzatto B, Momal A, et al. Long-term intensive care unit outbreak of carbapenemase-producing organisms associated with contaminated sink drains. J Hosp Infect 2024;143:38 – 47. https://doi.org/10.1016/j.jhin.2023.10.010.
8. Grota PG, Grant PS. Environmental infection prevention: priorities of patient safety collaboration. Crit Care Nurs Q 2018;41(1):38 – 46. https://doi.org/10.1097/CNQ.0000000000000184.
9. Browne K, White NM, Russo PL, Cheng AC, Stewardson AJ, Matterson G, et al. Investigating the effect of enhanced cleaning and disinfection of shared medical equipment on health-care-associated infections in Australia (CLEEN): a stepped-wedge, cluster randomised, controlled trial. Lancet Infect Dis 2024;24(12):1347 – 56. https://doi.org/10.1016/S1473-3099(24)00399-2.
10. Hassoun-Kheir N, Guedes M, Ngo Nsoga MT, Argante L, Arieti F, Gladstone BP, et al. A systematic review on the excess health risk of antibiotic-resistant bloodstream infections for six key pathogens in Europe. Clin Microbiol Infect 2024;30 Suppl 1:S14-25. http://dx.doi.org/10.1016/j.cmi.2023.09.001.
11. Kong Y, Liu T, Zhang YR, Wang H, Lin HY. Investigation of an outbreak of carbapenem resistant *Acinetobacter baumannii* in an intensive care unit during the COVID-19 epidemic. Antimicrob Resist Infect Control 2025;14(1):30. https://doi.org/10.1186/s13756-025-01547-0.
12. Doi Y, Murray GL, Peleg AY. *Acinetobacter baumannii*: evolution of antimicrobial resistance-treatment options. Semin Respir Crit Care Med 2015;36(1):85 – 98. https://doi.org/10.1055/s-0034-1398388.
13. Cheh-Oh N, Ungthammakhun C, Changpradub D, Santimaleeworagun W. The mortality of colistin monotherapy vs. colistin-sulbactam for carbapenem-resistant Acinetobacter baumannii pneumonia: a propensity score analysis. Infect Chemother 2025;57(1):138 – 47. https://doi.org/10.3947/ic.2024.0125.
14. Carling PC, Parry MM, Rupp ME, Po JL, Dick B, Von Beheren S, et al. Improving cleaning of the environment surrounding patients in 36 acute care hospitals. Infect Control Hosp Epidemiol 2008;29(11):1035 – 41. https://doi.org/10.1086/591940.

SUPPLEMENTARY MATERIAL

SUPPLEMENTARY TABLE 1. Clinical characteristics of CRAB infection in patients admitted to the ICU of a tertiary hospital.

Study ID	Bed no.	Age (year)/sex	Main underlying disease	Date of admission of ICU Date of discharge of ICU	Date of isolation	Other pathogens
XZ160601ABP007	08	76/M	Cerebral hemorrhage	May 25, 2016 June 6, 2016	June 1, 2016	CRKP
XZ160606ABP013 XZ160606ABP018	14	36/F	Multiple trauma	May 18, 2016 June 9, 2016	June 6, 2016	CRKP
XZ160620ABP012	13	53/F	Cerebral infarction	June 20, 2016 July 21, 2016	June 23, 2016	/
XZ190318ABP018	05	29/M	Brain stem hemorrhage	Mar 3, 2019 Mar 19, 2019	Mar 18, 2019	/
XZ190318ABP019	11	69/M	Multiple trauma	Mar 8, 2019 May 10, 2019	Mar 18, 2019	CRKP
XZ190318ABP020	01	69/F	Left basal ganglia hemorrhage	Mar 12, 2019 Mar 18, 2019	Mar 18, 2019	/
XZ190318ABP021	04	51/F	Postoperative cerebral hemorrhage	Mar 12, 2019 Mar 18, 2019	Mar 18, 2019	*Klebsiella Pneumoniae*
XZ190323ABP026	02	55/M	Multiple trauma	Mar 16, 2019 Apr l2, 2019	Mar 23, 2019	/
XZ191009ABP009	06	40/F	Middle cerebral artery aneurysm	Oct 3, 2019 Oct 10, 2019	Oct 9, 2019	/
XZ191010ABP001	09	45/M	Cerebral hemorrhage	Sep 9, 2019 Oct 15, 2019	Oct 10, 2019	CRKP
XZ191012ABP002	08	30/M	Diabetic ketoacidosis	Oct 8, 2019 Oct 18, 2019	Oct 12, 2019	CRKP
XZ191012ABP003	06	66/M	Upper gastrointestinal hemorrhage	Oct 5, 2019 Oct 14, 2019	Oct 12, 2019	/
XZ191012ABP005	18	48/F	Left cerebellar cerebral hemorrhage	Oct 10, 2019 Oct 24, 2019	Oct 12, 2019	CRKP
XZ191118ABP008	12	76/M	Multiple cerebral contusion	Nov 12, 2019 Nov 18, 2019	Nov 18, 2019	CRKP
XZ210909ABP005	22	79/M	Meningeoma	Sep 3, 2021 Sep 17, 2021	Sep 9, 2021	CRKP
XZ210910ABP001	23	64/M	Acute severe pancreatitis	Aug 30, 2021 Sep 29, 2021	Sep 10, 2021	/
XZ210910ABP002	18	80/M	Bilateral posterior communicating artery aneurysm	Aug 31, 2021 Sep 29, 2021	Sep 10, 2021	/
XZ210913ABP004	25	75/M	Type I respiratory failure	Sep 9, 2021 Sep 18, 2021	Sep 13, 2021	/
XZ210916ABP003	05	58/M	Intracranial hemorrhage(non-traumatic)	Sep 7, 2021 Oct 21, 2021	Sep 16, 2021	*Klebsiella Pneumoniae*

Abbreviation: CRAB=carbapenem-resistant *Acinetobacter baumannii*; CRKP=carbapenem-resistant *Klebsiella pneumoniae*; ICU=intensive care unit.

SUPPLEMENTARY TABLE S2. Summary of antibiotic susceptibility testing of *A. baumannii* clinical and environmental isolates from emergency ICU.

Study ID	Bed no. location/source	Drug resistance
XZ210910ABP001	23 sputum	TZA CTT CAZ FEP AZT IPM CIP LVX SXT TOB AMC DOR DOX MEM MXF TE TIC CXM SCF ZOX CTX CSSS PIP CPD NOR TIM
XZ160623ABP012	13 sputum	AMP SAM CRO FEP IPM GM TOB CIP LVX NIT SXT FOX AMC
XZ160606ABP018	14 exudate	AMP TZP CZ CRO FEP IPM GM TOB CIP LVX NIT SXT FOX AMC
XZ160601ABE010	18 computer mouse	AMP CZ CTT NIT
XZ160601ABE011	18 computer keyboard	AMP CZ CTT NIT
XZ191010ABP001	9 sputum	TZP CTT CAZ FEP AZT IPM CIP LVX SXT GM AMC DOR DOX MEM MXF TE CXM ZOX CTX CSSS PIP CPD
XZ191012ABP003	6 sputum	SAM CTT CAZ AZT IPM CIP LVX SXT TOB DOR MEM MXF TIC CXM SCF ZOX CTX CSSS PIP CPD
XZ191012ABP005	18 sputum	TZP CTT CAZ AZT IPM CIP LVX SXT GM AMC DOR MEM MXF CXM SCF ZOX CTX CSSS PIP CPD
XZ190318ABE015	23 glucometer cartridge	SAM TZP CAZ IPM GM CIP SXT MEM CTX AMK
XZ190318ABE016	24 bed rails	SAM TZP CAZ FEP IPM GM CIP LVX SXT MEM CTX AMK
XZ190319ABE003	5 surface of syringe pump	SAM TZP CAZ IPM GM CIP SXT MEM CTX AMK
XZ190319ABE004	17 ventilator valve	SAM TZP CAZ IPM GM CIP SXT MEM CTX AMK
XZ190319ABE007	19 writing trolley table top	SAM TZP CAZ FEP IPM GM CIP LVX SXT MEM CTX AMK
XZ210916ABP003	5 sputum	TAP CTT CAZ AZT IPM CIP LVX SXT TOB AMC DOR DOX MEM MXF TE TIC CXM ZOX CTX CSSS PIP CPD NOR TIM
XZ160601ABE001	13 treatment table handle	AMP SAM TZP CZ CTT CAZ CRO FEP AZT GM TOB CIP NIT SXT
XZ160601ABE003	23 bed rails	AMP SAM TZP CZ CTT CAZ CRO FEP AZT GM TOB CIP NIT SXT
XZ160601ABE004	11 ventilator buttons	AMP SAM TZP CZ CTT CAZ CRO FEP AZT GM TOB CIP NIT SXT
XZ160704ABE014	15 ventilator buttons	AMP SAM TZP CZ CTT CAZ CRO FEP AZT GM TOB CIP NIT SXT
XZ160601ABE005	2 therapeutic trolley table	AMP TZP CZ CTT CAZ CRO FEP AZT IPM GM TOB CIP LVX NIT SXT
XZ160704ABE015	8 bed rails	AMP SAM TZP CZ CTT CAZ CRO FEP AZT IPM GM TOB CIP NIT
XZ160606ABP013	14 abdominal drainage	AMP TZP CZ CRO FEP IPM GM TOB CIP NIT SXT AML FOX
XZ160601ABE006	23 ventilator air heater	AMP SAM TZP CZ CTT CAZ CRO FEP AZT IPM GM TOB CIP NIT SXT
XZ160601ABP007	8 sputum	AMP TZP CZ CRO FEP IPM GM TOB CIP LVX NIT SXT AML FOX
XZ160601ABE008	11 therapeutic trolley table	AMP SAM TZP CZ CTT CAZ CRO FEP AZT GM TOB CIP NIT SXT
XZ160704ABE016	8 writing desk	AMP SAM TZP CZ CTT CAZ CRO FEP AZT IPM GM TOB CIP NIT SXT
XZ160601ABE009	13 ventilator button	AMP SAM TZP CZ CTT CAZ CRO FEP AZT GM TOB CIP NIT SXT
XZ191012ABP002	8 blood	TZP CTT CAZ FEP AZT IPM CIP LVX SXT GM AMC DOR MEM MXF CXM SCF ZOX CTX CSSS PIP CPD
XZ190319ABE013	17 bed rails	SAM TZP CAZ IPM GM CIP LVX SXT MEM CTX AMK
XZ160704ABE017	8 cardiac monitor button	AMP SAM TZP CZ CTT CAZ CRO FEP AZT IPM GM TOB CIP LVX NIT SXT
XZ160601ABE002	23 ventilator connection	AMP SAM TZP CZ CTT CAZ CRO FEP AZT IPM GM TOB CIP NIT SXT
XZ160704ABE013	8 infusion pump	AMP SAM TZP CZ CTT CAZ CRO FEP AZT IPM GM TOB CIP NIT SXT
XZ210910ABP002	18 sputum	TZP CTT CAZ FEP AZT IPM CIP LVX SXT TOB AMC DOR DOX MEM MXF TE TIC CXM SCF ZOX CTX CSSS PIP CPD NOR TIM
XZ191118ABP008	12 sputum	TZP CTT CAZ FEP AZT IPM CIP SXT TOB AMC DOR DOX MEM MXF TE CXM ZOX CTX CSSS PIP CPD
XZ191009ABP009	6 sputum	TZP CAZ FEP AZT IPM CIP LVX MEM MIN SCF DOX
XZ190318ABP018	5 sputum	TZP CTT CAZ FEP AZT IPM CIP SXT DOR DOX MEM MXF TE TIC CXM SCF ZOX CTX CSSS PIP CPD
XZ190323ABP026	2 sputum	TZP CTT CAZ AZT IPM CIP LVX SXT TOB DOR MEM MXF TIC CXM SCF ZOX CTX CSSS PIP CPD
XZ191021ABE005	white coats	SAM TZP CAZ FEP IPM GM CIP SXT MEM SCF CTX AMK
XZ190318ABP019	11 sputum	TZP CTT CAZ FEP AZT IPM CIP SXT TOB DOR DOX MEM TE TIC CXM SCF ZOX CTX CSSS PIP CPD

Continued

Study ID	Bed no. location/source	Drug resistance
XZ190318ABP020	1 sputum	TZP CTT CAZ FEP AZT IPM CIP LVX SXT TOB DOR DOX MEM MXF TE TIC CXM SCF ZOX CTX CSSS PIP CPD
XZ190318ABP021	4 sputum	TZP CTT CAZ FEP AZT IPM CIP SXT TOB DOR DOX MEM MXF TE TIC CXM SCF ZOX CTX CSSS PIP CPD
XZ190318ABE002	5 bed rails	SAM TZP CAZ FEP IPM GM CIP SXT MEM SCF CTX AMK
XZ190319ABE005	17 syringe pump	SAM TZP CAZ FEP IPM GM CIP SXT MEM SCF CTX AMK
XZ190319ABE006	18 bed handle buttons	SAM TZP CAZ FEP IPM GM CIP SXT MEM SCF CTX AMK
XZ190318ABE008	16 bed rails	SAM TZP CAZ FEP IPM GM CIP SXT MEM SCF CTX AMK
XZ190321ABE009	21 writing trolley top	SAM TZP CAZ FEP IPM GM CIP SXT MEM SCF CTX AMK
XZ190318ABE011	14 PDA surface	SAM TZP CAZ FEP IPM GM CIP LVX SXT MEM SCF CTX AMK
XZ190318ABE012	14 bed rails	SAM TZP CAZ FEP IPM GM CIP SXT MEM SCF CTX AMK
XZ160704ABE019	15 cardiac monitor	AMP SAM TZP CZ CTT CAZ CRO FEP AZT IPM CIP NIT
XZ210915ABE001	6 bedside table	SAM TZP CAZ FEP IPM GM CIP LVX SXT MEM SCF CTX AMK
XZ210915ABE002	6 medical record folde	SAM TZP CAZ FEP IPM GM CIP LVX SXT MEM SCF CTX AMK
XZ210915ABE018	15 headboard	SAM TZP CAZ FEP IPM GM CIP LVX SXT MEM SCF CTX AMK
XZ191021ABE004	tap switch and spout	SAM TZP CAZ IPM GM CIP SXT MEM CTX AMK
XZ191021ABE010	nurse 3's hand (ungloved)	SAM TZP CAZ FEP IPM GM CIP LVX SXT PB MEM SCF CTX AMK
XZ191021ABE001	18 headboard	SAM TZP CAZ IPM GM CIP SXT MEM CTX AMK
XZ210913ABP004	25 sputum	TZP CTT CAZ FEP AZT IPM CIP LVX SXT TOB AMC DOR DOX MEM MXF TE TIC CXM SCF ZOX CTX CSSS PIP CPD NOR TIM
XZ210915ABE004	6 ventilator connection	SAM TZP CAZ IPM GM CIP LVX SXT MEM CTX
XZ210909ABP005	22 sputum	TZP CTT CAZ FEP AZT IPM CIP LVX TOB AMC DOR DOX MEM MXF TE TIC CXM ZOX CTX CSSS PIP CPD NOR TIM
XZ191021ABE006	drawer handles	SAM TZP CAZ FEP IPM GM CIP SXT MEM CTX AMK
XZ191021ABE007	door handles	SAM TZP CAZ FEP IPM GM CIP LVX SXT MEM SCF CTX AMK
XZ191021ABE009	nurse 1's hand (ungloved)	SAM TZP CAZ FEP IPM GM CIP LVX SXT MEM SCF CTX AMK

Abbreviation: AMP=ampicillin; SAM=ampicillin-sulbactam; TZP=piperacillin-tazobactam; CZ=cefazolin; CTT=cefotetan; CAZ=ceftazidime; CRO=ceftriaxone; FEP=cefepime; AZT=aztreonam; IPM=imipenem; GM=gentamicin; TOB=tobramycin; CIP=ciprofloxacin; LVX=levofloxaci; NIT=nitrofurantoin; SXT=trimethoprim-sulfamethoxazole; AML=amoxicillin; TGC=tigecycline; FOX=cefoxitin; AMC=amoxicillin-clavulantic acid; DOR=doripenem; DOX=doxycycline; PB=polymyxin B; MEM=meropenem; MIN=minocycline; MXF=moxifloxacin; TE=tetracycline; TIC=ticarcillin; CXM=cefuroxime; SCF=cefoperazone-sulbactam; ZOX=ceftizoxime; CTX=cefotaxime; CSSS=cefoperazone Sodium and Sulbactam Sodium; PIP=piperacillin; DOX=doxycycline; CPD=cefpodoxime; AMK=amikacin; NOR=norfloxacin; TIM=ticarcillin-clavulnic acid.

Methods and Applications

An Open-Source Data Driven Hybrid Modeling System for Infectious Disease Surveillance and Early Warning

Jianyi Zhang[1]; Haoliang Cui[1]; Yiwen Xing[1]; Zekun Wang[2]; Wenkai Luo[1]; Chaozhuo Wei[3]; Zhongwei Jia[1,#]

ABSTRACT

Introduction: The increasing trend of globalization has led to a heightened risk of imported epidemics; however, existing surveillance systems remain fragmented and reliant on laboratory confirmation. We developed an open-source data-driven hybrid modeling system to provide earlier and more reliable alerts, designed to complement China's multipoint trigger early-warning framework.

Methods: This system integrates heterogeneous signals, including official epidemiology, digital traces, mobility, meteorology, and pathogen genomics, using semantic harmonization and a hybrid analytic stack. Seasonality-adjusted baselines with anomaly detection, mobility- and climate-aware SEIR models, and short-horizon learners generated calibrated early-warning scores. Thresholds were constrained by positive predictive value. Pilot studies were conducted for coronavirus disease 2019 (COVID-19) in Yantai and severe fever with thrombocytopenia syndrome virus (SFTSV) in Shandong and Henan, with tuberculosis indicators embedded for programmatic use.

Results: Across deployments, the system achieved 83.3% sensitivity and 76.9% positive predictive value, providing a median lead time of 9.3 days before official confirmation. Forecasting accuracy reached 92.1% for COVID-19 in Yantai, 90.3% for SFTSV in Shandong, and 89.8% for SFTSV in Henan. Early warnings were aligned with subsequent confirmations and supported targeted screening and resource allocation.

Conclusion: An open-source data-driven hybrid modeling system can deliver calibrated and timely alerts across diverse pathogens. By broadening inputs, enabling cross-agency linkage, and offering operator-oriented dashboards, it serves as a practical complement to China's national early-warning system and has the potential for scaling out with One Health inputs.

Globalization and increased human mobility have raised the risk of infectious diseases. International tourist arrivals and global traffic have roughly doubled since 2000 (*1*). During the coronavirus disease 2019 (COVID-19) pandemic, imported cases repeatedly seeded local outbreaks in China, while the expanding distribution of severe fever with thrombocytopenia syndrome across East Asia illustrates cross border spread of vector-borne diseases (*2–3*). Tuberculosis (TB) remains a persistent global threat; with 10.6 million new cases and 1.3 million deaths in 2022; and rebounds in China underscore the need for improved prevention along travel corridors (*4–5*).

China has developed a nationwide surveillance backbone, including the National Notifiable Infectious Disease Reporting System (NIDRIS) and the China Infectious Disease Automated-alert and Response System (CIDARS) that provide direct case reporting and rule-based signal generation from statutory notifiable diseases (*6–7*). More recently, national guidance emphasizes multi-point trigger early-warning architecture aimed at integrating multiple data sources, enhancing interoperability, and supporting multi-agency collaboration (*8–9*). However, most current pilot studies and applications rely primarily on report-based analytics, such as space-time scan statistics, which identify spatiotemporal clusters but remain constrained by delayed confirmation, limited data inputs, and weak predictive power (*10–11*). These limitations reduce actionable lead time and restrict applicability to pathogens with long incubation periods or non-specific clinical presentations.

Epidemic intelligence research has explored statistical, mechanistic models, and machine learning approaches separately; however, few studies combine them in hybrid frameworks balancing interpretability and accuracy (*12–13*). Existing studies often lack interoperability standards and operator-facing dashboards, limiting their scalability and usability in real-world decision-making environments.

To address these gaps, we introduce an open-source data-driven hybrid modeling system designed to complement China's national multi-point-trigger early-warning architecture. The system integrates heterogeneous open and partner-shared signals — including epidemiological reports, digital traces, mobility, meteorology, and pathogen genomics — through semantic harmonization and hybrid analytics, including seasonality-adjusted baselines, anomaly detection, mobility- and climate-aware SEIR models, and short-horizon sequence learners. Interoperable HL7 FHIR-aligned data contracts enable scalable integration with health, customs, and laboratory systems (*14*). While operator-oriented dashboards follow established design principles for interpretability and oversight (*15*). We present the system's architecture and pilot evidence across COVID-19 and severe fever with thrombocytopenia syndrome virus (SFTSV) and show how the same framework embeds TB indicators for programmatic use, bridging open-source data intelligence with the national early-warning workflow.

METHODS

We selected three pathogen targets to test the system's One Health versatility across distinct transmission modes and timescales: COVID-19 (acute respiratory disease requiring rapid community forecasting), SFTSV (vector-borne disease requiring ecological integration), and tuberculosis (chronic disease requiring long-term strategic planning). The pilot sites were chosen based on disease burden and data feasibility; for SFTSV, Shandong and Henan provinces were selected as high-endemicity regions in China, providing sufficient case volume to validate vector-driven models. For COVID-19, Yantai was selected as a representative coastal port city that experienced distinct waves of local transmission triggered by importation. This setting offered clear onset-to-suppression dynamics essential for validating the community forecasting model's sensitivity to intervention measures. The system continuously ingests heterogeneous data, performs semantic harmonization, runs hybrid analytics (statistical baselines, mechanistic models, and deep-sequence learners), and emits a calibrated early warning score (EWS) for operations. Personally identifiable information was not collected or processed (Figure 1).

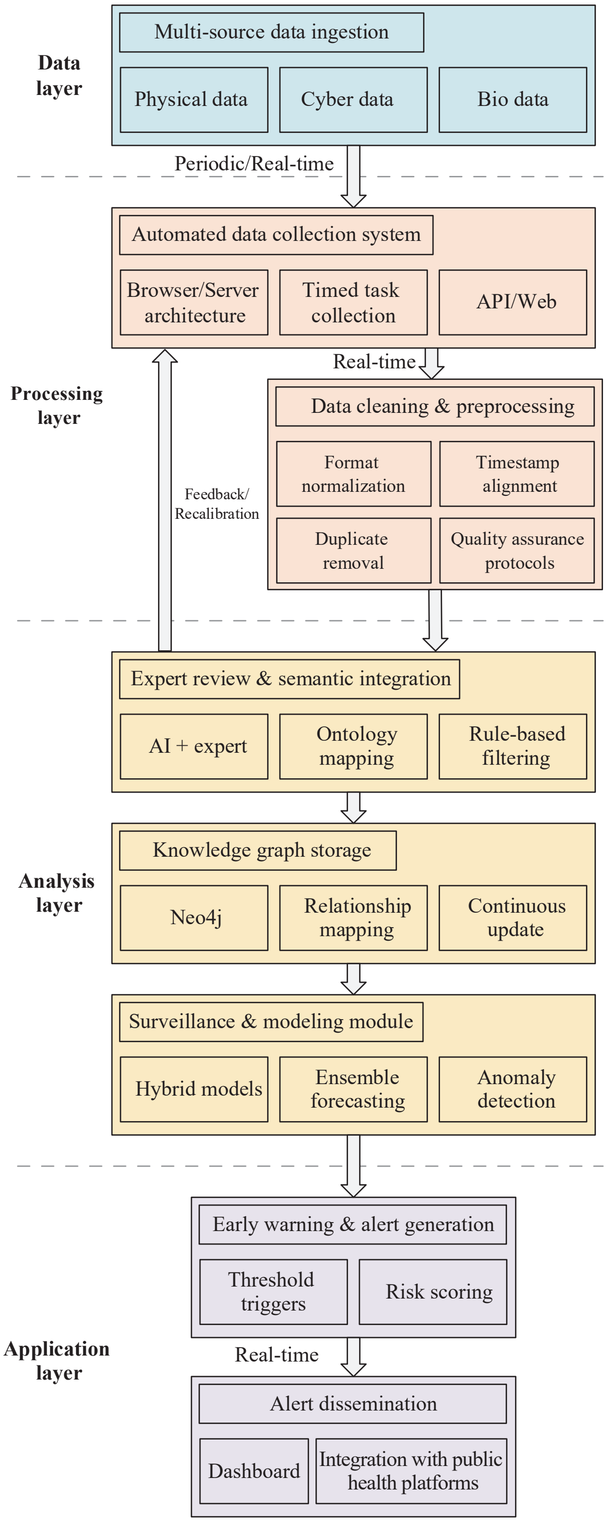

FIGURE 1. Workflow from data ingestion to alert dissemination.

Data Sources and Preprocessing

In this study, the term "open-source data" refers to open-source intelligence (OSINT) and publicly available datasets that are accessible without proprietary restrictions. These include official bulletins, digital signals, meteorological records, and anonymized mobility data, distinct from internal hospital records or confidential line-list data.

Official epidemiology relies on national/provincial bulletins and WHO/ECDC situation updates; digital epidemiology integrates multichannel digital traces such as search engine queries (Baidu Index, Wikipedia Pageviews), social media discussions (Weibo), and content from aggregators (Douyin/TikTok China, Toutiao), all equipped with geotags and temporal stamps; genomics provides sequence metadata for pathogen context; context & covariates encompass human mobility, meteorology, and holiday markers; and for the vector signal SFTSV, national tick index surveillance data is digitized from official graphs using scale-mean abstraction to create daily or weekly exogenous drivers, with monthly series derived through calendar aggregation.

Model Development Methodology

In this study, we developed three distinct model components integrated through a hybrid framework, with detailed methodologies provided in the supplementary materials. The SFTSV model utilizes a network transmission approach where the vector driver is approximated by a Fourier series fitted to the 2018–2019 national tick index, assuming stationary seasonal phenology. For the COVID-19 model, an agent-based SEIR model was implemented on a dynamic contact graph; biological parameters were fixed to literature values to ensure identifiability, focusing calibration solely on the effective contact probability. Rifampicin-resistant tuberculosis (RR-TB) incidence was estimated following the WHO-recommended mathematical procedure (Supplementary Table S1, available at https://weekly.chinacdc.cn). Finally, these outputs were integrated via hybrid fusion, employing logistic stacking as a meta-learner to weigh mechanistic and deep learning signals based on their historical performance.

RESULTS

System-level Alert Performance

Across pilots, the system operated at a pre-specified threshold tuned for decision utility (PPV constraint ≥ 0.70). Against officially confirmed events, the system achieved 83.30% sensitivity and 76.90% positive predictive value (PPV), with a median lead time of 9.30 days before first confirmation. Alerts and confirmatory timelines are illustrated in the dashboard traces (Figure 2E–F); adjudication logs indicate that most false positives arose from short sub-threshold anomalies that did not consolidate into confirmed events (Table 1).

Site-level Forecasting Performance

For SFTSV monthly incidence forecasting in Shandong and Henan, the model's predictions closely tracked observed trends in both provinces, as illustrated in Figure 3A–B. Using the pre-specified accuracy metric with bootstrap 95% confidence intervals (*CI*s), Shandong (2013–2015) achieved 90.29% accuracy (95% *CI*: 85.79%, 93.84%). Henan (2009–2014; including Xinyang) achieved 89.81% (95% *CI*: 86.24%, 93.08%).

Peak months and troughs aligned with the seasonality captured by the mechanistic (tick- and human-driven) transmission terms, and the model reproduced the interannual amplitude differences without overfitting (Figure 2A–B).

In the COVID-19 community forecasting conducted for Yantai, community-scale forecasts achieved 92.15% accuracy (95% *CI*: 86.99%, 93.96%) under the same definition. In peak-focused validation with 10,000 simulations (Poisson-drawn initial seeds within the 95% interval), the model achieved a peak timing accuracy of 88.43% (95% *CI*: 88.26%, 88.59%) and a peak magnitude accuracy of 91.16% (95% *CI*: 91.04%, 91.30%). The forecast trajectories and observed counts are shown in Figure 2C–D.

At the PPV-constrained threshold, the median lead time was 9.3 days (overall). Most detected events had ≥ 7 days' advance notice; short-lead alerts (<7 days) clustered in late-season periods with compressed confirmation cycles (timeline examples in Figure 3E).

Our TB model, adapted from the recurrent framework of Li (*5*), closely reproduced historical trends (R^2=0.95 for total incidence, 0.99 for RR-TB incidence, and 0.82 for TB deaths), with a posterior mean force of infection of 2.35 per year (95% *CI*: 1.16, 3.58). Projections to 2030 indicated an incidence rate of 33.7 per 100,000 (95% *CI*: 30.80, 38.30), below Li's estimate of 44.9 but above the End TB target of 13, suggesting China's 2024–2030 goal (43) is attainable. The model was implemented as an interactive Shiny application to support visualization and policy use.

DISCUSSION

This study demonstrates that the system can combine diverse open signals with hybrid models to

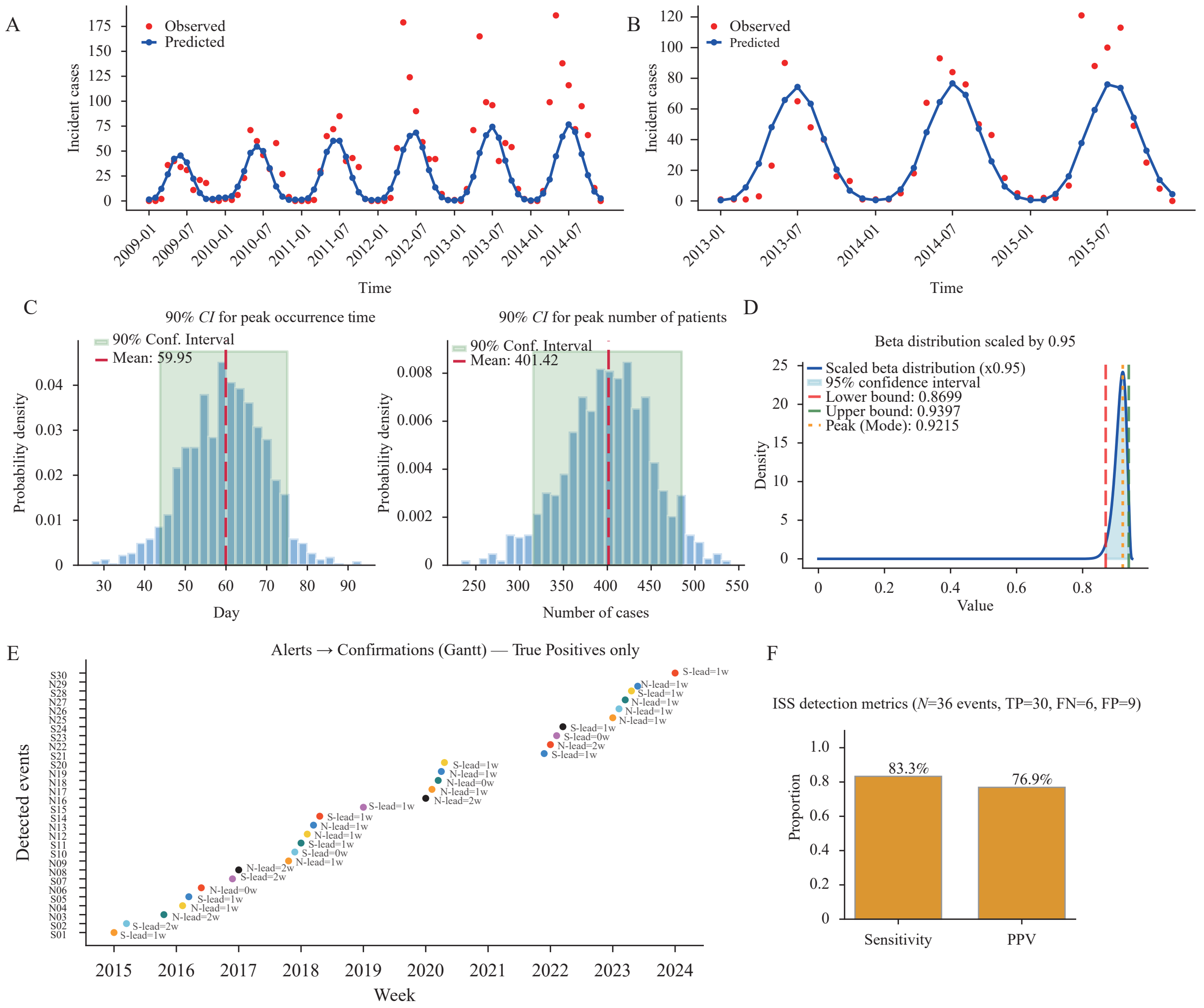

FIGURE 2. Model performance across pilots. (A) Monthly SFTSV cases in Henan (2009–2014); (B) Monthly SFTSV cases in Shandong (2011–2015). (C) Posterior distributions of COVID-19 predicted outcome intervals; (D) Beta-distributed probability calibration for COVID-19 with 95% confidence intervals; (E) System alerts and official confirmations for true-positive events; (F) Aggregate detection metrics including sensitivity and positive predictive value.

Abbreviation: PPV=positive predictive value; SFTSV=severe fever with thrombocytopenia syndrome virus; *CI*=confidence interval; TP=true positive; FN=false negative; FP=false positive; COVID-19=coronavirus disease 2019.

produce calibrated early-warning scores constrained by positive predictive values, reducing false alerts while preserving sensitivity. We tested three pathogen contexts — COVID-19, SFTSV, and TB — and observed their practical utility in both acute and chronic use cases.

Semantic harmonization organized multi-source evidence into consistent geotemporal units, reducing ambiguity in sparse or fast-moving events. Hybrid modeling integrated statistical baselines, mobility- and climate-aware SEIR models (including a human-tick-human pathway for SFTSV), and short-horizon learners to preserve epidemiologic interpretability while capturing nonlinearity. PPV-constrained probability calibration translated model outputs into actionable alerts, improving resource allocation and limiting alert fatigue. Together, these choices enabled earlier, more precise alerts that aligned well with observed trends without overfitting to site-specific conditions.

Relationship to Prior Work and Added Value

While frameworks such as EWARS support outbreak management (*8*–*9*), their reliance on statutory reports limits their timeliness (*6*). Previous studies have often traded interpretability (statistical baselines) for short-term accuracy (machine learning), frequently lacking multisource integration. Our system advances the field by 1) hybridizing statistical, mechanistic, and sequence-based learners to balance

TABLE 1. System- and site-level performance summary.

Setting	Pathogen	Outcome granularity	Detection sensitivity, %	PPV, %	Median lead time, days	Forecast accuracy, % (95% *CI*)	Peak timing accuracy, % (95% *CI*)	Peak magnitude accuracy, % (95% *CI*)	$R^2_{totalincidence}$	$R^2_{RR-TBincidence}$	$R^2_{TBdeaths}$
Overall (all pilots)	Mixed	Event-level alerts	83.3	76.9	9.3						
Yantai, Shandong	COVID-19	Community time series				92.15 (86.99, 93.96)	88.43 (88.26, 88.59)	91.16 (91.04, 91.30)			
Shandong	SFTSV	Monthly incidence				90.29 (85.79, 93.84)	–	–			
Henan	SFTSV	Monthly incidence				89.81 (86.24, 93.08)	–	–			
China (National)	TB	National annual incidence							0.95	0.99	0.82

Note: "−" means no data. The indicators of TB are presented in the form of proportions.
Abbreviation: COVID-19=coronavirus disease 2019; SFTSV=severe fever with thrombocytopenia syndrome virus; *CI*=confidence interval; TB=tuberculosis.

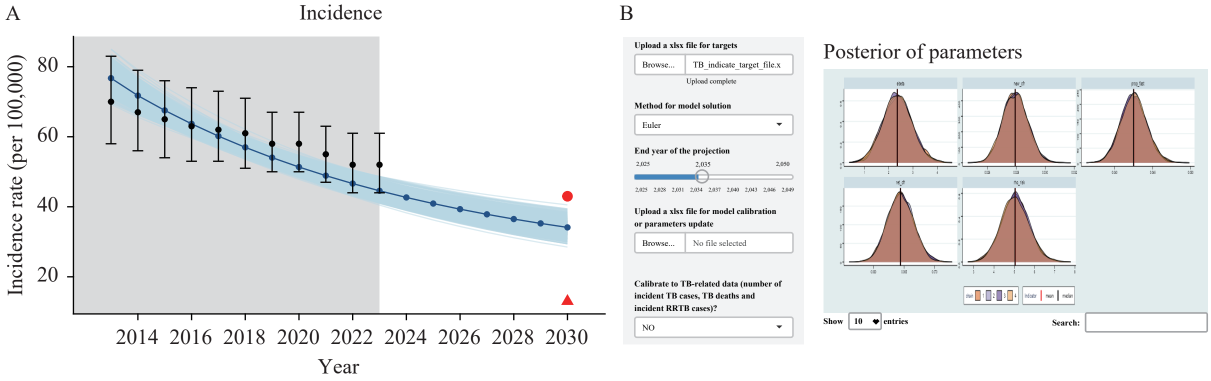

Upload a xlsx file for targets
TB_indicate_target_file.x
Upload complete
Method for model solution
Euler
End year of the projection
2,025 2,035 2,050
2,025 2,028 2,031 2,034 2,037 2,040 2,043 2,046 2,049
Upload a xlsx file for model calibration or parameters update
No file selected
Calibrate to TB-related data (number of incident TB cases, TB deaths and incident RRTB cases)?
NO
Show 10 entries

FIGURE 3. Dashboard (TB). (A) Incidence Trends and Projections; (B) Posterior Parameters and Model Application
Note: The system showed high stability in robustness checks under parameter perturbations.
Abbreviation: TB=tuberculosis.

interpretability with adaptability; 2) integrating open signals beyond statutory notifications; and 3) achieving high predictive accuracy and meaningful lead times relative to uncalibrated systems.

Qualitatively, the hybrid framework offers distinct advantages over the single-method baselines. Mechanistic SEIR models capture long-term seasonal trends but lag during stochastic onsets, whereas deepsequence learners offer high sensitivity but lack epidemiological transparency. By fusing these approaches, our system stabilizes forecasts during peaks while improving sensitivity during early onsets. Quantitatively, the system demonstrated a median lead time of 9.3 days relative to official confirmation. Given the inherent reporting lags in traditional passive surveillance (*7*), this represents a substantial window for pre-emptive intervention.

Pathogen Landscape Perspective

A modular design allows flexible application across pathogen contexts. The same framework generates outbreak alerts for COVID-19 and SFTSV while embedding TB analytics to strengthen screening and continuity of care. This adaptability enables emergency response and long-term control through a unified operational surface.

Operational utility differs across pathogen types. For acute outbreaks, such as COVID-19 and SFTSV, the system functions as a tactical early-warning tool, issuing short-horizon alerts (lead time <14 days) to trigger immediate containment measures such as targeted screening or vector control. For chronic diseases such as TB, the system serves a strategic forecasting function, projecting long-term trends (e.g., to 2030) to guide resource allocation and policy target setting. This multimodal capability aligns with the tiered surveillance architecture advocated in recent national guidance on intelligent multi-point trigger systems (*8*–*9*).

Implications for Public Health Practice

Embedding such a system into an operational setting can accelerate detection, improve the allocation of quarantine and laboratory resources, and better align vector control with clinical responses during high-risk periods. These functions align with national guidance on building a multipoint-trigger early-warning architecture (*8*–*9*) and with international calls to strengthen public health forecasting (*12*). The system also benefits from interoperable data contracts, such as HL7 FHIR, which facilitate scalable integration across health, customs, and laboratory agencies (*14*), as well as operator-oriented dashboards designed for real-time decision support (*15*). In the short term, priorities include regular recalibration, expanded data exchange with partner agencies, and the incorporation of operator feedback loops. In the medium term, multisite evaluations are required to provide robust evidence of improved timeliness and efficiency.

First, data-related issues exist in multiple aspects. Digital traces are susceptible to “media noise”, and smartphone-derived mobility data may underrepresent the elderly. Meanwhile, meteorological data face spatiotemporal alignment challenges. Second, there are ecological and modeling-related constraints. The national tick index has limited local granularity in terms of ecological constraints. Structural simplifications, assuming uniform mixing for COVID-19 or simplified vector-host cycles for SFTSV, may overlook microenvironmental heterogeneity. Finally, there are coverage and parameter-related problems. Pilot coverage was geographically limited, and parameter uncertainty persists as PPV thresholds need recalibration and TB models depend on uncertain latent progression parameters.

Conflict of Interest: No conflicts of interest.

Funding: Supported by the National Natural Science Foundation of China (72274210, 72174004).

doi: 10.46234/ccdcw2026.036

Corresponding author: Zhongwei Jia, jiazw@bjmu.edu.cn.

---

[1] Department of Global Health, School of Public Health, Peking University, Beijing, China; [2] Beijing Municipal Health Big Data and Policy Research Center, Beijing, China; [3] Division of Surveillance, Early Warning and Emergency Response, Heilongjiang Provincial of Disease Control and Prevention, Harbin City, Heilongjiang Province, China.

Submitted: October 11, 2025
Accepted: February 09, 2026
Issued: February 20, 2026

REFERENCES

1. Yu XJ, Liang MF, Zhang SY, Liu Y, Li JD, Sun YL, et al. Fever with thrombocytopenia associated with a novel bunyavirus in China. N Engl J Med 2011;364(16):1523 – 32. https://doi.org/10.1056/NEJMoa1010095.
2. Cui HL, Shen SJ, Chen L, Fan ZY, Wen Q, Xing YW, et al. Global epidemiology of severe fever with thrombocytopenia syndrome virus in human and animals: a systematic review and meta-analysis. Lancet Reg Health West Pac 2024;48:101133. https://doi.org/10.1016/j.lanwpc.2024.101133.
3. Miao D, Dai K, Zhao GP, Li XL, Shi WQ, Zhang JS, et al. Mapping the global potential transmission hotspots for severe fever with thrombocytopenia syndrome by machine learning methods. Emerg Microbes Infect 2020;9(1):817 – 26. https://doi.org/10.1080/22221751.2020.1748521.
4. World Health Organization (WHO). Global tuberculosis report 2023. Geneva: WHO; 2023. https://www.who.int/publications/i/item/9789240083851.
5. Li T, Zhang B, Du X, Pei SJ, Jia ZW, Zhao YL. Recurrent pulmonary tuberculosis in China, 2005-2021. JAMA Netw Open 2024;7(8):e2427266. https://doi.org/10.1001/jamanetworkopen.2024.27266.
6. Sun HM, Hu WH, Wei YY, Hao YT. Drawing on the development experiences of infectious disease surveillance systems around the world. China CDC Wkly 2024;6(41):1065 – 74. https://doi.org/10.46234/ccdcw2024.220.
7. Ren X, Wang LP, Cowling BJ, Zeng LJ, Geng MJ, Wu P, et al. Systematic review: national notifiable infectious disease surveillance system in China. Online J Public Health Inform 2019;11(1):e62534. https://doi.org/10.5210/ojphi.v11i1.9897.
8. National Bureau of Disease Control and Prevention, National Health Commission of the People’s Republic of China, National Development and Reform Commission, Ministry of Education of the People’s Republic of China, Ministry of Civil Affairs of the People’s Republic of China, Ministry of Finance of the People’s Republic of China, et al. Guiding opinions on the establishment of a sound and intelligent multi-point trigger infectious disease surveillance and early warning system. 2024. https://www.gov.cn/zhengce/zhengceku/202408/content_6971481.htm. (In Chinese).
9. Yang WZ, Lan YJ, Lyu W, Leng ZW, Feng LZ, Lai SJ, et al. Establishment of multi-point trigger and multi-channel surveillance mechanism for intelligent early warning of infectious diseases in China. Chin J Epidemiol 2020;41(11):1753 – 57. https://doi.org/10.3760/cma.j.cn112338-20200722-00972.
10. Liu QQ, Li JH, Liu SY, Tang L, Wang XQ, Huang AD, et al. The Epidemiological Characteristics and Spatiotemporal Clustering of Measles—China, 2005-2022. China CDC Wkly 2024;6(27):665 – 9. https://doi.org/10.46234/ccdcw2024.123.
11. Levin-Rector A, Kulldorff M, Peterson ER, Hostovich S, Greene SK. Prospective spatiotemporal cluster detection using SaTScan: tutorial for designing and fine-tuning a system to detect reportable communicable disease outbreaks. JMIR Public Health Surveill 2024;10:e50653. https://doi.org/10.2196/50653.
12. Lutz CS, Huynh MP, Schroeder M, Anyatonwu S, Dahlgren FS, Danyluk G, et al. Applying infectious disease forecasting to public health: a path forward using influenza forecasting examples. BMC Public Health 2019;19(1):1659. https://doi.org/10.1186/s12889-019-7966-8.
13. Reich NG, Brooks LC, Fox SJ, Kandula S, McGowan CJ, Moore E, et al. A collaborative multiyear, multimodel assessment of seasonal influenza forecasting in the United States. Proc Natl Acad Sci USA 2019;116(8):3146 – 54. https://doi.org/10.1073/pnas.1812594116.
14. Vorisek CN, Lehne M, Klopfenstein SAI, Mayer PJ, Bartschke A, Haese T, et al. Fast Healthcare Interoperability Resources (FHIR) for interoperability in health research: systematic review. JMIR Med Inform 2022;10(7):e35724. https://doi.org/10.2196/35724.
15. Rabiei R, Bastani P, Ahmadi H, Dehghan S, Almasi S. Developing public health surveillance dashboards: a scoping review on the design principles. BMC Public Health 2024;24(1):392. https://doi.org/10.1186/s12889-024-17841-2.

SUPPLEMENTARY MATERIAL

DATA PROCESSING LAYER CONSTRUCTION

As illustrated in the Processing Layer of Figure 1, the system follows a two-stage construction protocol. 1) Automated Data Collection: Built on a Browser/Server (B/S) architecture, utilizing timed task collection modules to continuously ingest data via public APIs and web-scraping interfaces. 2) Data Cleaning & Preprocessing: Raw inputs undergo a standardized pipeline: 1) Format Normalization parses heterogeneous text/JSON into structured schemas; 2) Timestamp Alignment synchronizes all records to UTC+8; 3) Duplicate Removal eliminates redundant entries via hash matching; and 4) Quality Assurance Protocols (e.g., winsorization) filter outliers to ensure data integrity. Source-region normalization was performed using a Z-score with a small ridge.

$$\tilde{x}_{s,t,r} = \frac{x_{s,t,r} - \mu_{s,r}}{\sigma_{s,r} + \varepsilon} \tag{1}$$

MODEL DEVELOPMENT METHODOLOGY

SFTSV Network Transmission Model (Human-Tick-Human)

Tick Index as a Seasonal Driver: A Fourier series approximates the tick index$\mathrm{TickIndex}(t)$to capture the annual and biannual cycles:

$$\mathrm{TickIndex}(t) = A_0 + A_1 \sin(\omega t) + B_1 \cos(\omega t) + A_2 \sin(2\omega t) + B_2 \cos(2\omega t) \tag{2}$$

estimated using the nonlinear least-squares method. This driver transmits the force of infection from the tick into a human channel.

The monthly observed incidence $\{Y_k\}_{k=1}^{n}$ was modeled as a Poisson variable, with the mean $\lambda_k(\theta)$ implied by the state equations:

$$\begin{gathered} Y_k \sim \mathrm{Pois}(\lambda_k(\theta)), \\ \log \mathcal{L}(\theta) = \sum_{k=1}^{n} \log(\mathrm{Pois}(Y_k \mid \lambda_k) + 10^{-7}). \end{gathered} \tag{3}$$

where the small constant prevents numerical underflow. Posterior computation uses a grid/maximum A Posteriori (MAP) strategy with log-posterior stabilization:

$$P(\theta \mid D) \propto \exp\left(\log P(D \mid \theta) + \log P(\theta) - \max_{\theta'} \log P(D \mid \theta')\right) \tag{4}$$

followed by normalization and MAP selection. Sensitivity checks use a random-start local search over the prior box.

We utilized 2018–2019 national tick surveillance data to derive a normalized seasonal function of vector activity. The use of this later-period index to drive the historical model (2009–2015) is consistent with long-term epidemiological observations, indicating that vector phenology follows relatively stable annual cycles driven by climatic factors. Based on this, we assumed that the seasonal shape remained stationary, while allowing the transmission amplitude to fit dynamically to the observed incidence in each year.

COVID-19 Community Network Model (agent SEIR on Dynamic Contact Graph)

Resident Classes: Residents were grouped according to mobility patterns: 1) fixed workplace/school (regular, high-frequency travel), 2) no fixed workplace/retired/home-based (variable patterns), and 3) low mobility (elderly/children).

Graph construction. Each household is a node with attributes (demography, mobility propensity). Edges represent residential proximity (within unit/building/compound). During simulation, edges are dynamically augmented by co-presence in venues (workplace/school, transit, shops/parks/clinics), forming a time-varying multilayer graph.

A semi-mechanistic approach was adopted to ensure parameter identifiability. Biological parameters were fixed based on established literature: the mean latent period was set to 5.2 days and the infectious period to 5.8 days.

Agents transitioned between compartments (Susceptible-Exposed-Infectious-Recovered) based on these fixed intervals and a time-varying force of infection derived from the dynamic contact graph. Consequently, the model calibration focused solely on estimating the effective contact probability (β_t) and the initial seed size, thereby reducing dimensionality and preventing overfitting.

Estimation of Incidence of RR-TB (Rifampicin-Resistant Tuberculosis)

Total tuberculosis incidence $I(t)$ was obtained from the compartmental model as

$$I(t) = \omega_{fast} \cdot E_{fast}(t) + \omega_{slow} \cdot E_{slow}(t) + \rho \cdot R(t) \tag{5}$$

We then applied the mathematical procedure recommended by the World Health Organization to derive the incidence of rifampicin-resistant (RR) TB, expressed by the following equation:

$$I_{rr}(t) = I(t)[(1 - f) \cdot p_{new}(t) \cdot ((1 - r(t)) + r(t) \cdot \rho_{RRTB}) + f \cdot p_{ret}(t)] \tag{6}$$

Deep sequence Learners and Fusion

Parallel sequence models (LSTM/temporal CNN) use multistream inputs$X_{t,i}$(normalized signals, recent cases, mobility, and meteorology) to predict h-step-ahead counts:

$$\hat{y}_{t+h,i} = g_{\omega}([X_{t-w+1,i}, \ldots, X_{t,i}]) \tag{7}$$

trained with a Huber loss and correlation-promoting regularizer:

$$\mathcal{J} = \sum_{t,i} \mathcal{L}\left(y_{t,i}, \hat{y}_{t,i}\right) - \lambda \operatorname{corr}\left(y_{\cdot,i}, \hat{y}_{\cdot,i}\right) \tag{8}$$

Outputs from statistical baselines, mechanistic models, and learners were Platt-scaled to calibrated probabilities $p_{t,i}^{(m)}$ and fused by logistic stacking.

$$\Pr(\text{event}_{t,i} = 1) = \sigma\left(\alpha_0 + \sum_m \alpha_m \operatorname{logit} p_{t,i}^{(m)}\right) \tag{9}$$

An EWS combines stacked risk with anomaly flags:

$$\text{EWS}_{t,i} = \sum_m w_m \tilde{p}_{t,i}^{(m)} + \eta_1 \{S_{t,i} > h\} + \eta_2 \max(Z_{t,i}, 0), \tag{10}$$

and triggers when $\text{EWS}_{t,i} \geq \tau$. Threshold τ is tuned to maximize F_1 under a minimum PPV constraint (PPV≥ 0.70) using rolling-origin evaluation.

The logistic stacking layer functions as a meta-learner that assigns dynamic weights to the component models based on their historical validation performance. This mechanism is designed to reconcile conflicting signals; for instance, the system tends to assign higher weights to mechanistic SEIR outputs during stable seasonal periods (capturing regular trend lines), while upweighting digital signals and deep learners during irregular onset phases, where statistical anomalies precede official reporting. This dynamic weighting strategy aligns with the principles of ensemble model averaging, in which component models are weighted according to their predictive performance in specific contexts.

Semantic Harmonization and Knowledge Graph

An NLP pipeline performs named-entity and relation extraction over unstructured text and bulletins and mapping to controlled vocabulary (disease/syndrome, host/vector, place, and intervention). Entities and relations populate a knowledge graph $G = (V, E)$ that 1) resolves aliases and administrative hierarchies (district→city→province), 2) stores provenance, and 3) serves efficient retrieval for modeling features and operator dashboards.

Statistical Baselines and Anomaly Detection

Syndromic/aggregate counts $Y_{t,r}$ are modeled using a seasonality-adjusted quasi-Poisson Generalized Linear Model (GLM) with trend and holiday effects; standardized residuals feed a one-sided Cumulative Sum (CUSUM) to generate anomaly evidence:

$$Y_{t,r} \sim \mathrm{QP}(\lambda_{t,r}), \log \lambda_{t,r} = \beta_0 + \beta_1 t + f_{\mathrm{seas}}(t) + \gamma^\top H_t + \delta_r \tag{11}$$

$$Z_{t,r} = \frac{Y_{t,r} - \hat{\lambda}_{t,r}}{\sqrt{\widehat{\mathrm{Var}}(Y_{t,r})}}, S_{t,r} = \max\{0, S_{t-1,r} + Z_{\mathrm{t,r}} - k\}, \mathit{alert\ if} S_{t,r} > h \tag{12}$$

SFTSV Network Transmission Model (Human-Tick-Human) Calculation Details

Human–tick–human force of infection. Let S_t, E_t, I_t, R_t, D_t denote human compartments, $N_t = S_t + E_t + I_t + R_t$ The total infection pressure is the sum of tick to human and human to human components:

$$\lambda_t = \beta_{th}(t)\frac{S_t}{N_t}\mathrm{TickIndex}(t) + \beta_{hh}(t)\frac{S_t I_t}{N_t} \tag{13}$$

Seasonal/behavioral modulation of transmission:

$$\begin{aligned} \beta_{hh}(t) &= 10^{b_h}, \\ \beta'_{th}(t) &= 10^{b_t}\frac{\sin(\alpha_t t/365 + 2\pi\phi/365) + 1}{2}. \end{aligned} \tag{14}$$

where $\beta'_{th}(t)$ absorbs the proportionality constant K between the observed tick index and effective contacts (only $\beta'_{th}(t)$ is estimated).

State evolution (discrete-time):

$$\begin{aligned} S_{t+1} &= S_t - \lambda_t, \\ E_{t+1} &= E_t + \lambda_t - \sigma E_t, \\ I_{t+1} &= I_t + \sigma E_t - \mu I_t - \delta I_t, \\ R_{t+1} &= R_t + \delta I_t, \\ D_{t+1} &= D_t + \mu I_t. \end{aligned} \tag{15}$$

Here σ is progression from exposed to infectious (latent-to-infectious rate), δ is recovery, μ is disease-induced mortality (fixed from guidelines/meta-analysis as literature-based constants for the baseline run).

Bayesian parameter estimation. We estimate b_h, b_t, α_t, ϕ under weakly informative uniform priors (reflecting seasonality and scale).

$$\begin{aligned} b_h &\sim \mathrm{Unif}(-10, -6), \\ b_t &\sim \mathrm{Unif}(-10, -6), \\ \alpha_t &\sim \mathrm{Unif}(5.98, 6.61), \\ \phi &\sim \mathrm{Unif}(10, 100). \end{aligned} \tag{16}$$

COVID-19 Community Network Model (agent SEIR on Dynamic Contact Graph) Calculation Details

Two transmission phases. Phase-1 (lockdown/home isolation), household droplets and environment/aerosol exposures dominate; Phase-2 (reopening) includes venue-specific contacts (work/school, transit, leisure). Let $\mathcal{N}_i^{\mathrm{home}}$ represent household neighbors, $\mathcal{M}$ venue types, $c_{im}(t)$ expected contacts, and $\pi_{im}(t)$ time fraction in the venue $m; \eta$ vaccine effectiveness (susceptibility reduction). The probability of infection for node i on day t is modeled as:

$$p_i^{(1)}(t) = 1 - (1 - \eta)\underbrace{\exp(-\rho_{\mathrm{env}}\tau_i^{\mathrm{home}}(t))}_{\text{no env. infection}}\underbrace{\prod_{j \in \mathcal{N}_i^{\mathrm{home}}}(1 - \rho_{\mathrm{home}}\{I_j(t) = 1\}),}_{\text{no household infection}} \tag{17}$$

$$p_i^{(2)}(t) = 1 - (1 - \eta)\exp(-\rho_{\mathrm{env}}\tau_i(t))\prod_{j \in \mathcal{N}_i^{\mathrm{home}}}(1 - \rho_{\mathrm{home}}\{I_j(t) = 1\})\prod_{m \in \mathcal{M}}(1 - \rho_m)^{c_{im}(t)\pi_{im}(t)}. \tag{18}$$

Here, $\rho.$ is the per-contact transmission probability, and τ denotes the time in the environment. The state evolution follows the agent-level SEIR with daily updates.

$$\begin{aligned}
&X_i(t) \in \{S, E, I, R\},\\
&\Pr\{X_i(t+1) = E \mid X_i(t) = S\} = p_i(t),\\
&\Pr\{X_i(t+1) = I \mid X_i(t) = E\} = \sigma,\\
&\Pr\{X_i(t+1) = R \mid X_i(t) = I\} = \gamma.
\end{aligned} \tag{19}$$

and vaccination acts as a multiplicative susceptibility reduction $(1-\eta)$. For network-level inference, a cavity/percolation recursion approximates the probability that infection does not traverse edge $j \to i$ up to time t:

$$\begin{aligned}
\psi_{j\to i}(t) &= \prod_{k\in\mathcal{N}(j)i} [1-\beta_{jk}(1-\psi_{k\to j}(t-1))],\\
\pi_i(t) &= 1-\prod_{j\in\mathcal{N}(i)} [1-\beta_{ij}(1-\psi_{j\to i}(t))].
\end{aligned} \tag{20}$$

which improves stability on large graphs.

Estimation of Incidence of RR-TB (Rifampicin-Resistant Tuberculosis) Calculation Details

Tuberculosis natural history. The compartmental model employed to represent the natural history of TB largely replicates the structure proposed by Li et al., with only minor modifications. We reimplemented the model in Stan, a probabilistic programming language written in C++, to situate the analysis of tuberculosis and other infectious diseases within a coherent Bayesian framework. This model distinguishes between two latency pathways: fast (E_{fast}) and slow ($\mathrm{E}_{\mathrm{slow}}$). As no consensus on the definition of fast-progressing latent infection exists in the literature, we adopted the progression parameters reported by Menzies et al., which are also used by the WHO. The annual rate of progression from the fast-progression latent compartment to active tuberculosis (ω_{fast}) was set at 0.0826 per person-year, whereas the corresponding rate for the slow-progression latent compartment (ω_{slow}) was fixed at 0.0006 per person-year. Disease status was classified into two groups based on the WHO guidance issued in 2013: newly diagnosed TB (I_{new}) and retreated TB (I_{ret}). Although the 2024 WHO revision refers to the latter category as being re-registered for treatment, the retreated designation was retained in the present analysis. Future iterations of the model will adopt the updated terminology. Individuals who were cured or completed their treatment were transferred to the compartment, represented as recovery (R). Individuals in compartment R remain at risk of recurrence and can return to an infectious state (I_{ret}). The model equations are as follows:

$$\begin{aligned}
\frac{dS}{dt} &= B\cdot N - \beta\frac{S(I_{new}+I_{ret})}{N} - M\cdot S,\\
\frac{dE_{fast}}{dt} &= (1-g)\cdot\beta\frac{S(I_{new}+I_{ret})}{N} - \omega_{fast}\cdot E_{fast} - M\cdot E_{fast},\\
\frac{dE_{slow}}{dt} &= g\cdot\beta\frac{S(I_{new}+I_{ret})}{N} - \omega_{slow}\cdot E_{slow} - M\cdot E_{slow},\\
\frac{dI_{new}}{dt} &= \omega_{fast}\cdot E_{fast} + \omega_{slow}\cdot E_{slow} - (M + CFR_{new})\cdot I_{new} - \eta_{new}\cdot I_{new} - f_{new}\cdot I_{new},\\
\frac{dI_{ret}}{dt} &= f_{new}\cdot I_{new} + f_{new}\cdot I_{new} + \rho\cdot R - (M + CFR_{ret})\cdot I_{ret} - \eta_{ret}\cdot I_{ret},\\
\frac{dR}{dt} &= \eta_{new}\cdot I_{new} + \eta_{ret}\cdot I_{ret} - M\cdot R - \rho\cdot R.
\end{aligned} \tag{21}$$

Data flux and model calibration. Gao et al. estimated that the prevalence of LTBI in China in 2013 was 18.08%, corresponding to approximately 247 million infections. Houben and Dodd estimated that there were 350 million infections in China in 2014. We rely on the estimation conducted by Gao et al. because it is derived from large-scale empirical data collected in China and, therefore, aligns more closely with the study population and methodological framework. Therefore, our model-fitting starting point was set to 2013.

Robustness Checks

The performance estimates were stable in the rolling-origin evaluation under small perturbations of priors for the SFTSV transmission modifiers and venue contact parameters for COVID-19. Bootstrap confidence intervals

SUPPLEMENTARY TABLE S1. RR-TB calculation parameters and explanations.

Description	Definition	Value
B	Birth rate	Birth rates were modelled using logistic regression. $\mathrm{logit}(B) = \ln\frac{B}{1-B} = b_{0,B} + \mathrm{b}_B\mathrm{t}$ Differentiating the implied logistic curve with respect to time gives the corresponding ordinary differential equation $\frac{dB}{dt} = \mathrm{b}_B\mathrm{B}(1-B)$
M	Background mortality rate	Background mortality rates were modelled using logistic regression. $\mathrm{logit}(M) = \ln\frac{M}{1-M} = b_{0,M} + \mathrm{b}_M\mathrm{t}$ Differentiating the implied logistic curve with respect to time gives the corresponding ordinary differential equation $\frac{dM}{dt} = \mathrm{b}_M\mathrm{M}(1-M)$
β	Transmission rate	Calibrated to match epidemiological data, with uniform priors [0, 30].
g	Proportion of infected individuals that transition into the "slow" progression LTBI compartment	Fixed, 0.91
ω_{fast}	The annual rate of progression from the "fast" progression LTBI to active TB.	Fixed, 0.0826
ω_{slow}	The annual rate of progression from the "slow" progression LTBI to active TB.	Fixed, 0.0006
CFR_{new}	Case fatality rate for newly diagnosed patients	Calibrated to match epidemiological data, with uniform priors [0, 0.2].
CFR_{ret}	Case fatality rate for retreated patients	Calibrated to match epidemiological data, with uniform priors [0, 0.2].
η_{new}	Treatment success rate for newly diagnosed patients	Region varying. For China, the overall value was 0.94.
η_{ret}	Treatment success rate for retreated patients	Region varying. For China, the overall value was 0.85.
f_{new}	Treatment failure rate for newly diagnosed patients	Region varying. For China, the overall value was 0.0227.
f_{ret}	Treatment failure rate for retreated patients	Region varying. For China, the overall value was 0.0527.
ρ	Overall recurrence rate	Region varying. For China, the overall value was 0.0047.
$\mathrm{r}(\mathrm{t})$	The proportion of recurrent cases out of the sum of new and recurrent cases at time t.	Computed from the model as $\mathrm{r}(\mathrm{t}) = \frac{\rho \cdot \mathrm{R}(\mathrm{t})}{\mathrm{I}(\mathrm{t})}$
f	The cumulative risk that an incident case undergoes a non-relapse retreatment, defined as retreatment following treatment failure or return after default.	f_{new} was used as a proxy for f.
$p_{new}(t)$	The estimated proportions of RR-TB among newly diagnosed patients at time t.	Different from the methods used by WHO, we constructed logistic regression to estimate the proportions. $\mathrm{logit}(p_{new}(t)) = \ln\frac{p_{new}(t)}{1-p_{new}(t)} = \mathrm{b}_{0,new} + \mathrm{b}_{new}\mathrm{t}$
$p_{ret}(t)$	The estimated proportions of RR-TB among retreated patients at time t.	Different from the methods used by WHO, we constructed logistic regression to estimate the proportions. $\mathrm{logit}(p_{ret}(t)) = \ln\frac{p_{ret}(t)}{1-p_{ret}(t)} = \mathrm{b}_{0,ret} + \mathrm{b}_{ret}\mathrm{t}$
ρ_{RRTB}	The risk of RR-TB in recurrent cases relative to previously untreated cases.	Calibrated to match epidemiological data, with uniform priors [1, 10].

Abbreviation: LTBI=latent tuberculosis infection; TB=tuberculosis.

overlapped across sites, and alert metrics were consistent when restricted to weeks with complete multisource coverage.

Uncertainty Quantification

We addressed the parameters and predictive uncertainty using distinct approaches tailored to each model component. For the mechanistic SFTSV and TB models, we employed a Bayesian framework and reported parameter estimates with 95% credible intervals (CrIs) derived from the posterior distributions. For the COVID-19 community model and deepsequence learners, where analytical posteriors were intractable, we utilized bootstrap resampling (N=2,000 iterations) to generate 95% confidence intervals (*CIs*) for all predictive horizons.

Evaluation Plan

Event Matching and Definitions: An ‘event match’ was defined as a system alert (EWS > threshold) occurring within a 14-day window preceding the official confirmation date of a case cluster. To account for confirmation delays, the official date was adjusted by subtracting the median reporting lag (2 days for COVID-19 and 5 days for SFTSV) derived from the historical NIDRIS data. Multiple alerts triggered within a single window were aggregated into a single ‘detected event’ to prevent double-counting. Forecast agreement (SFTSV monthly): Accuracy was defined as $(1 - \text{NMAE}) \times 100\%$ with 95% bootstrap CIs. Although standard statistical evaluations typically use RMSE or MAE, we adopted this percentage-based metric to facilitate intuitive interpretation by public health operators. This choice prioritizes communicative utility in operational dashboards over strict statistical conventions, which is consistent with the user-centered design principles in public health surveillance.

$$\begin{aligned} \text{Sensitivity} &= \frac{\text{TP}}{\text{TP} + \text{FN}}, \\ \text{PPV} &= \frac{\text{TP}}{\text{TP} + \text{FP}}, \\ \text{Specificity} &= \frac{\text{TN}}{\text{TN} + \text{FP}}. \end{aligned} \tag{22}$$

$$\text{Brier} = \frac{1}{n} \sum_{t,i} \left(p_{t,i} - y_{t,i}\right)^2 \tag{23}$$

$$\begin{aligned} \text{NMAE} &= \frac{\frac{1}{n} \sum_{k=1}^{n} \left|y_k - \hat{y}_k\right|}{\max(y) - \min(y)}, \\ \text{Accuracy} &= (1 - \text{NMAE}) \times 100\%. \end{aligned} \tag{24}$$

Review

Current Status of Clade 2.3.4.4b H5N1 Highly Pathogenic Avian Influenza Virus Transmission in Mammals

Chuanxiu Li[1]; Xinru Lyu[1]; Xiang Li[1]; Zhongwei Jia[2,#]; Hongliang Chai[1,#]

ABSTRACT

Since late 2020, clade 2.3.4.4b H5N1 highly pathogenic avian influenza viruses (HPAIVs) have expanded globally, infecting wild birds, poultry, and an increasing range of mammals. Sustained transmission has occurred in minks and dairy cattle, accompanied by key polymerase basic 2 (PB2) mutations (e.g., E627K, D701N), signaling mammalian adaptation and heightened zoonotic risk. From 2021 to early 2025, 82 human cases, including fatalities in China and the US, underscored rising public health concerns, although no sustained human-to-human transmission has been detected. This review summarizes the epidemiology, transmission dynamics, and molecular evolution of clade 2.3.4.4b H5N1 in mammals. Large-scale outbreaks in US dairy cattle and associated human cases highlight significant cross-species risks, while China's high poultry vaccination coverage, rapid culling, and nationwide surveillance demonstrate the value of proactive prevention. These contrasting experiences emphasize the need for targeted surveillance, reinforced biosecurity, accelerated countermeasure development, and global coordination under the One Health framework.

Since the emergence of highly pathogenic avian influenza virus (HPAIV) H5N1 in Guangdong Province, China, in 1996, it has evolved into multiple genetic clades through ongoing mutation and reassortment (*1*). In October 2020, a novel clade 2.3.4.4b H5N1 HPAIV, resulting from reassortment between H5N8 HPAIVs and European HxN1 low pathogenic avian influenza viruses (LPAIVs), was first detected in wild ducks in the Netherlands (*2*). Its extensive spread among wild birds and poultry, driven by migratory birds, has caused unprecedented ecological and economic impacts (*3*).

Since 2021, clade 2.3.4.4b H5N1 HPAIVs have increasingly been detected in diverse mammalian hosts (*4*). Several isolates harbor key amino acid substitutions associated with enhanced mammalian adaptation (*5*), indicating improved host compatibility. Recently, infections in dairy cattle in the United States (US), accompanied by human cases linked to direct animal contact, have highlighted a novel transmission route (*6*). This development signals a potential breach of established host barriers and underscores the need for heightened vigilance regarding zoonotic risks (*7*).

This review synthesizes current knowledge of clade 2.3.4.4b H5N1 HPAIV infections in mammals, emphasizing epidemiological trends, links to human cases, and mechanisms of cross-species transmission. Its aim is to inform surveillance, risk assessment, and prevention strategies for both animal and human health.

RISING TRENDS OF MAMMALIAN AND HUMAN INFECTIONS

From 2021 to 2025, surveillance data from the Food and Agriculture Organization of the United Nations (FAO), the World Health Organization (WHO), and the World Organization for Animal Health (WOAH) indicate a marked increase in clade 2.3.4.4b H5N1 HPAIV infections in mammals, accompanied by sporadic human cases (*4*). During this period, 71 mammalian species across 32 countries were affected, with both host diversity and geographic range expanding annually (Figure 1 and Supplementary Table S1, available at https://weekly.chinacdc.cn/).

In 2021, mammalian infections were primarily confined to Europe and involved a limited number of species. By 2023, cases had spread extensively across North and South America, Europe, and parts of Antarctica, representing the maximum observed species diversity and geographic spread. Although the overall range stabilized in 2024–2025, new host species, such as small rodents and additional domestic animals, were identified, indicating ongoing viral adaptation and

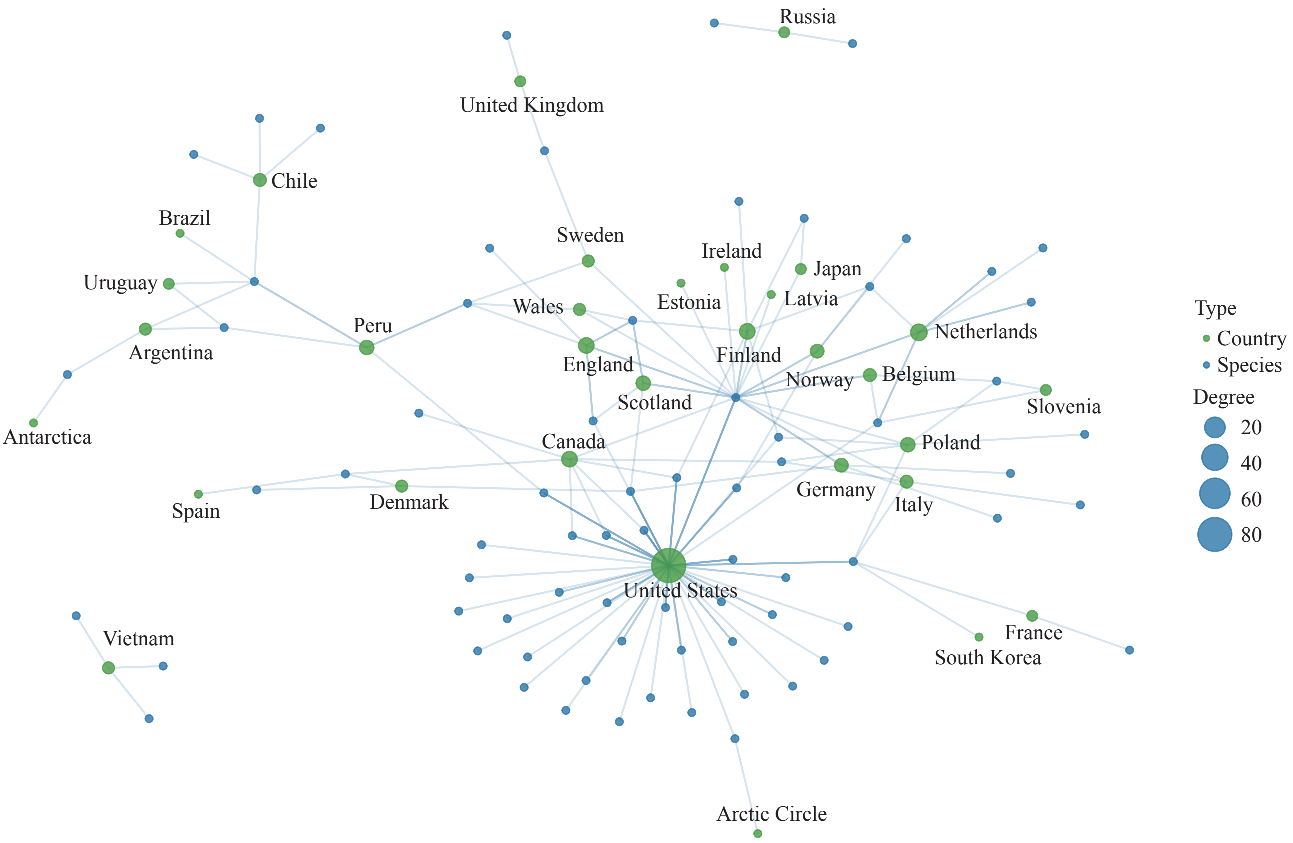

FIGURE 1. Network of avian influenza virus spread across countries and host species.
Note: Green nodes represent host species, and blue nodes represent countries. Node size reflects the degree (number of documented host–country connections). Edges indicate confirmed reports of H5N1 infection in a specific host species within a given country. The network is literature-based and not derived from viral genomic sequence data. It was constructed using the host–country occurrence dataset summarized in Supplementary Table S1 and generated in R (version 4.4.3), R Foundation for Statistical Computing, Vienna, Austria.
Abbreviation: USA=United States of America; UK=United Kingdom.

ecological persistence.

Recurrent infections were documented in certain species, notably marine mammals (e.g., sea lions, seals), farmed carnivores (e.g., minks), and wild carnivores (e.g., red fox, *Vulpes vulpes*) (Figure 2). Genetic analyses identified key mutations associated with mammalian adaptation, suggesting enhanced replication efficiency in these hosts and raising concerns about increased zoonotic potential.

Between 2021 and February 2025, 82 confirmed human infections with clade 2.3.4.4b H5N1 HPAIVs were reported across Asia, the Americas, and Europe, including two fatal cases (China and the US) (Figure 3). Although rare, such infections have attracted growing attention (*8*). Most cases involved direct or indirect contact with infected animals (*9*), coinciding with the detection of H5N1 HPAIVs in US dairy cattle in 2024 (*10*) (Figure 4). To date, there is no evidence of sustained human-to-human transmission, underscoring the importance of continued genomic surveillance in both animal and human populations.

NOTABLE INFECTIONS IN MAMMALS

Terrestrial Wild Mammals

Due to its wide distribution, frequent predation on wild birds, and high clinical detectability, the red fox is the most commonly reported terrestrial wild mammal infected with clade 2.3.4.4b H5N1 HPAIVs, serving as a sentinel species for mammalian surveillance (*11*). Since 2021, infections have been documented across Europe, North America, and Asia, including the Netherlands, Finland, Poland, the US, Canada, and Japan (*12*–*14*).

In the Netherlands (May 2021–December 2022), foxes, polecats, otters, martens (*15*), and badgers were infected with clade 2.3.4.4b H5N1 HPAIVs that were

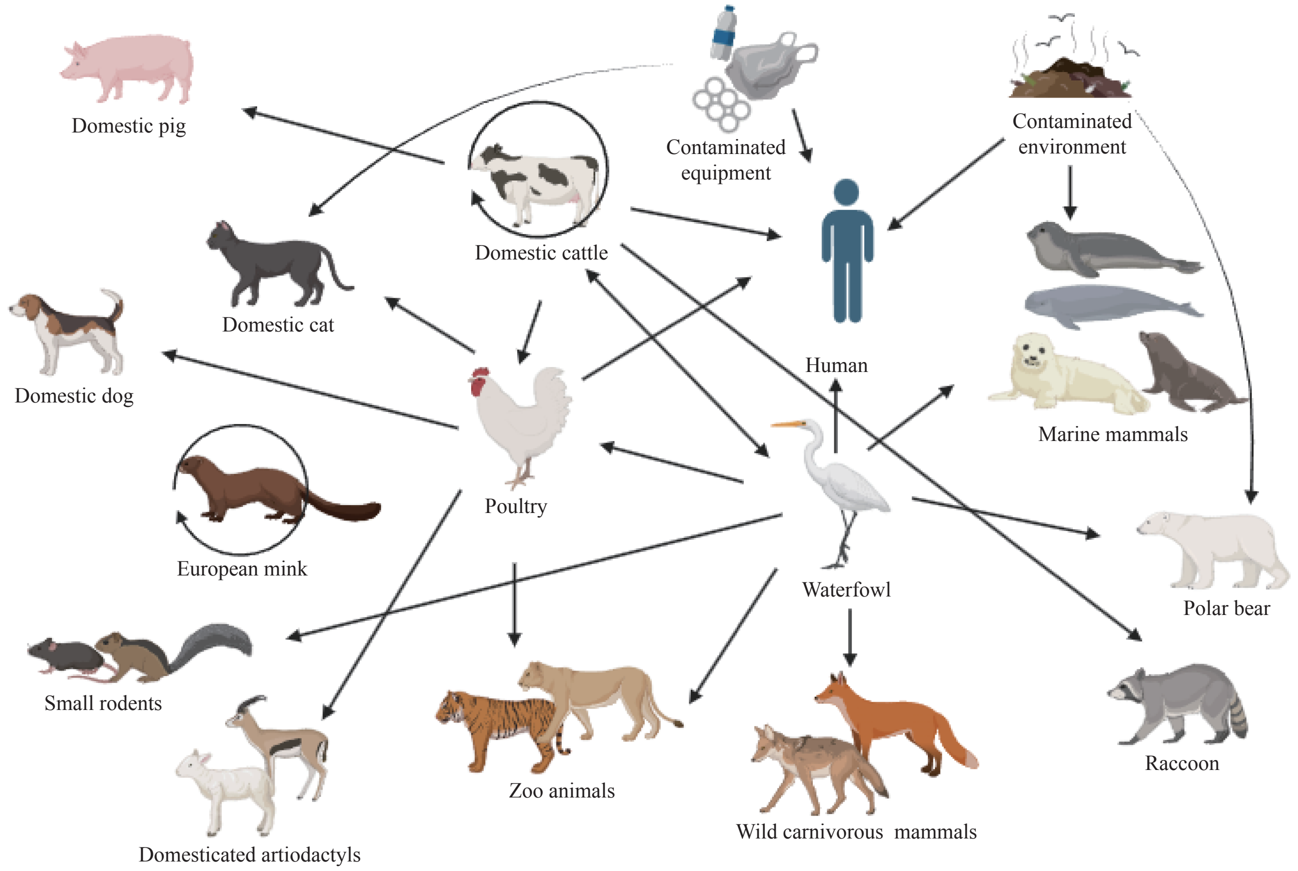

FIGURE 2. Transmission pathways of clade 2.3.4.4b H5N1 HPAIVs between humans and animal hosts.
Note: Arrows represent potential transmission directions supported by evidence reported in peer-reviewed literature or official outbreak investigations. Only pathways with documented epidemiological, environmental, or behavioral links, such as direct contact, predation or scavenging, shared environments, or spillover from infected poultry, were included. The figure illustrates cross-species transmission dynamics and associated public health risks. It was created with BioRender.com (https://biorender.com).
Abbreviation: HPAIVs=highly pathogenic avian influenza viruses.

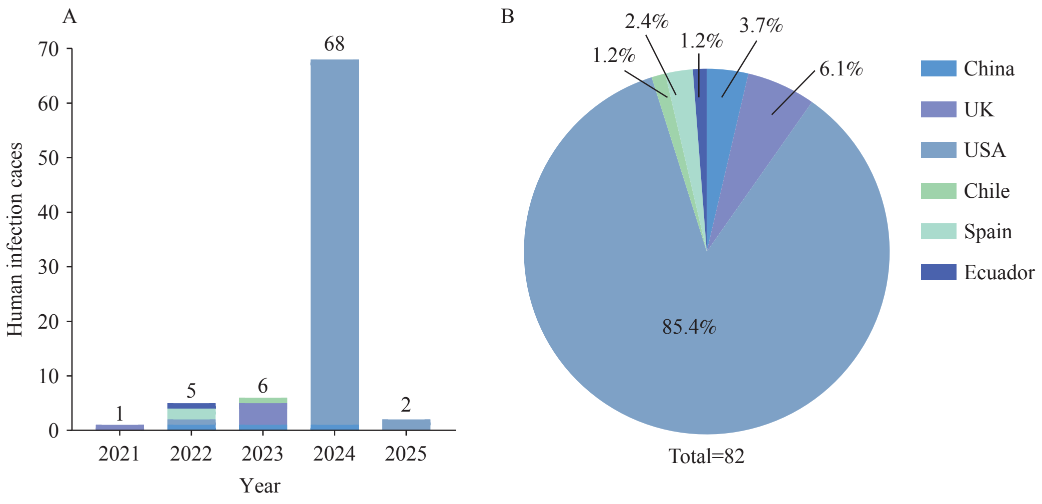

FIGURE 3. Epidemiology of human infections with clade 2.3.4.4b H5N1 HPAIVs, 2021–2025. (A) Number of human infection cases by year, 2021–2025. (B) Geographical distribution of human infection cases, 2021–2025 (*N*=82).
Abbreviation: HPAIVs=highly pathogenic avian influenza viruses; USA=United States of America; UK=United Kingdom.

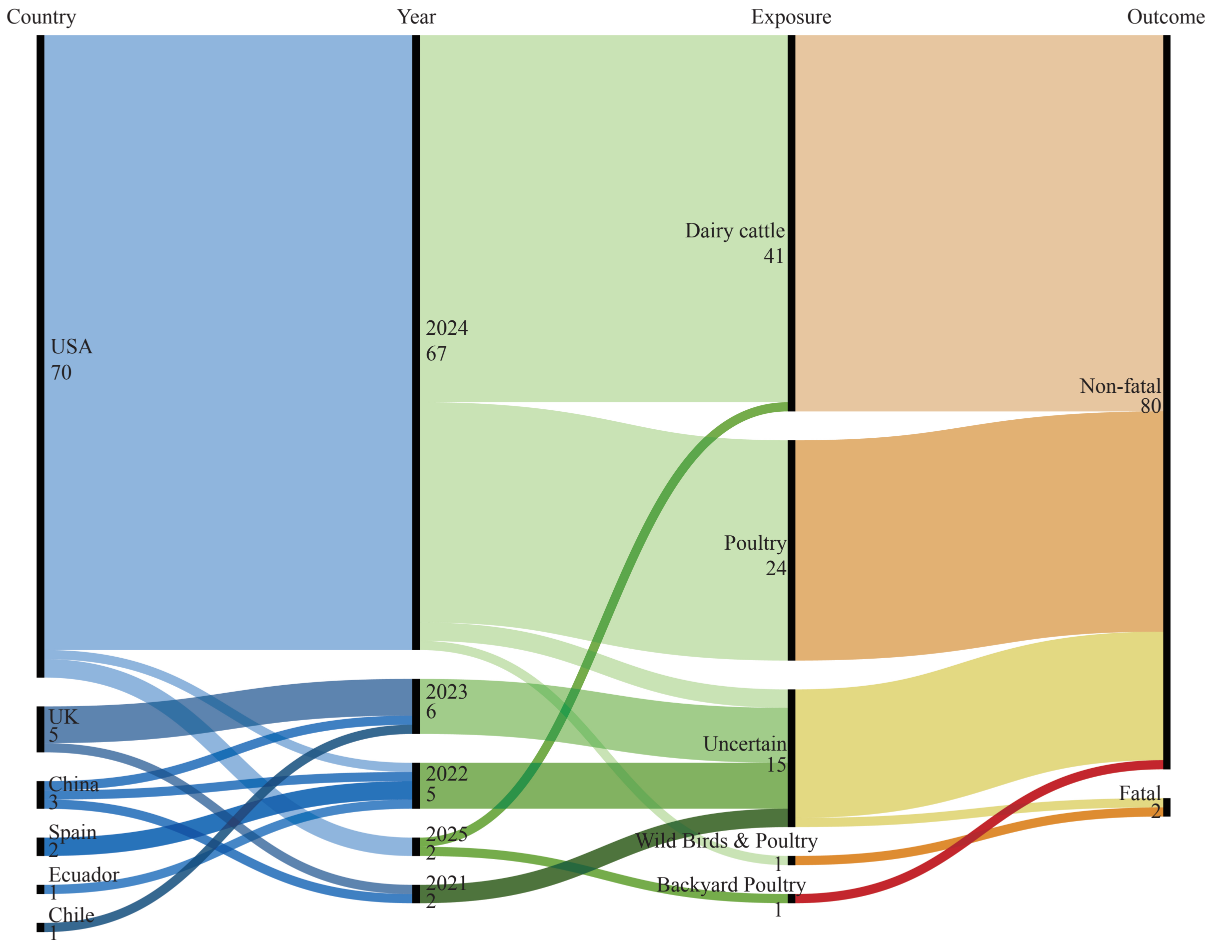

FIGURE 4. Associations between mammalian H5N1 HPAIVs outbreaks and human cases.
Note：It was created with GraphPad Prism 9.5.0, GraphPad Software, San Diego, California, USA. Associations are established based on temporal and spatial co-occurrence of outbreaks in mammals and human infections reported in the literature or official surveillance data. Only confirmed human cases with documented exposure to infected mammals or affected farms are included. This figure does not imply direct causality but illustrates potential exposure pathways. It was created with RAWGraphs 2.0. https://app.rawgraphs.io/.
Abbreviation: HPAIVs=highly pathogenic avian influenza viruses; USA=United States of America; UK=United Kingdom.

genetically similar to local avian strains. Several fox and polecat isolates carried the polymerase basic 2 (PB2) E627K mutation, indicative of mammalian adaptation (*16*). In Canada (2021–2022), foxes exhibited severe neurological disease with meningoencephalitis and pneumonia, confirming neurotropism (*17*). In the US (2022), 67 wild carnivores from 10 states, including foxes, skunks, raccoons (*Procyon lotor*), bobcats (*Lynx rufus*), coyotes (*Canis latrans*), and fishers (*Pekania pennanti*), tested positive for clade 2.3.4.4b H5N1 HPAIVs (*18*), with many presenting with central nervous system lesions (*12*).

Habitat overlap among infected carnivores, wild birds, and areas of human activity may increase environmental contamination and incidental human exposure.

Farmed and Domestic Mammals

In October 2022, farmed minks in Spain experienced a clade 2.3.4.4b H5N1 outbreak with the PB2 T271A mutation, demonstrating efficient farm-level transmission; minks can act as “mixing vessels” for avian and human influenza viruses (*7*,*18*). Control measures included culling, enhanced biosecurity, and staff monitoring (*19*). In June 2023, multiple felids in Poland were infected with related viruses, showing rapid disease progression and severe respiratory and neurological symptoms (*20*). Since 2022, clade 2.3.4.4b H5N1 has caused fatal infections in domestic cats across Europe and North America, posing zoonotic risks through direct or indirect exposure (*18*). Most cases involved predation on infected birds or poultry (Figure 2), although some occurred without clear outdoor contact, suggesting alternative transmission routes (*21*). There is no evidence that sustained cat-to-cat transmission is a major pathway (*22*). Only isolated cases and experimental data exist, with no systematic culling or official control measures. Clear policy guidance and transparent response strategies are needed.

In October 2024, clade 2.3.4.4b H5N1 HPAIVs were detected in US pigs without evidence of sustained transmission (*22*) and for the first time in goats (*Capra aegagrus hircus*) (*23*) and alpacas (*Lama glama*) (*24*), likely resulting from cohabitation with infected poultry. Continued surveillance of domestic mammals, particularly felines and pigs, is essential given their potential roles in viral adaptation and transmission to humans (*25*).

Marine Mammals

Since 2021, clade 2.3.4.4b H5N1 HPAIVs have caused unprecedented mortality events among marine mammals across multiple coastal regions (*26*). Early cases included a harbor porpoise (*Phocoena phocoena*) in Sweden in June 2022, followed by large outbreaks in harbor seals (*Phoca vitulina*) and gray seals (*Halichoerus grypus*) along the northeastern US and eastern Canada, temporally coinciding with massive seabird die-offs (*27*). In 2023, widespread outbreaks affected marine mammals in South America and Antarctica, including sea lions, fur seals, and southern elephant seals, likely facilitated by migratory seabirds (Figure 2), resulting in historic multi-country mortality events (*28*). Viral isolates from Peru and Chile harbored mammalian-adaptive PB2 mutations (D701N and Q591K), indicating enhanced viral adaptation and suggesting the potential for sustained circulation within marine ecosystems (*29*).

Control efforts rely on surveillance, protection, and public education, as no vaccines or antiviral drugs are available. Dense seabird and pinniped aggregations in Antarctica pose a risk for outbreaks (*30*), and the presence of mammalian-adaptive mutations raises concerns about possible transmission among marine mammals.

THE US DAIRY CATTLE OUTBREAK AND ASSOCIATED HUMAN INFECTIONS

Although clade 2.3.4.4b H5N1 infections in China remain limited, international outbreaks provide valuable lessons. Large-scale epidemics in US dairy cattle and associated human cases offer key insights into viral adaptation, transmission, and public health response, informing efforts to strengthen early warning systems and emergency preparedness in China.

Since March 2024, clade 2.3.4.4b H5N1 HPAIVs have been detected in more than 13,000 wild birds, 175 million poultry, and over 1,000 dairy herds across 17 US states (*31*). Dairy cattle, previously considered largely resistant to influenza A viruses (IAVs), were found to be susceptible following the emergence of genotypes B3.13 and D1.1, both capable of efficient infection in lactating cows (*32*). Molecular analyses traced B3.13 to wild birds, followed by spread to wildlife and poultry. The virus has been identified in unpasteurized milk, with some cows remaining asymptomatic, suggesting silent transmission (*33*). In response, authorities implemented targeted testing, movement restrictions, milk handling and pasteurization protocols and enhanced biosecurity measures for farm personnel, effectively mitigating further spread (*34*).

From February 2024 to June 2025, 70 human infections were reported in the US, including one fatal case. Most cases were linked to direct contact with infected dairy cattle, poultry, or backyard flocks, confirming animal-to-human transmission (*35*). Genetic analyses identified D1.1 as the predominant lineage, closely related to dairy cattle and poultry isolates, and several human cases carried mammalian-adaptive PB2 mutations, suggesting ongoing adaptation (*36*). These findings underscore the importance of integrated surveillance and coordinated interventions.

ZOONOTIC POTENTIAL AND EMERGING RISKS OF H5N1

The WHO notes that H5N1 viruses are widespread among wild birds and poultry worldwide and occasionally cause human infections. Most human cases are associated with contact with infected birds or contaminated environments, with no evidence of sustained human-to-human transmission (*37*). Clade 2.3.4.4b viruses pose cross-species transmission risks, necessitating multi-species surveillance, strengthened biosecurity, vaccine development, and comprehensive risk management. China emphasizes high vaccination coverage, rapid culling, and nationwide monitoring (*38*), while international efforts focus on farm-level control measures (*19*,*34*).

Under a One Health framework, global strategies should integrate cross-species surveillance, biosecurity, risk communication, and occupational protection to prevent zoonotic transmission and safeguard both human and animal health.

Conflicts of interest: No conflicts of interest.

Acknowledgements: We also gratefully acknowledge the contributions and dataprovided by the following institutions: the UK Government (Department for Environment, Food & Rural Affairs); the US Department of AgricultureAnimal and Plant Health Inspection Service (USDAAPHIS); the European Food Safety Authority (EFSA); the European Centre for Disease Prevention and Control (ECDC); the World Animal HealthInformation System (WAHIS); the Center forInfectious Disease Research and Policy (CIDRAP); the Ministry of Agriculture and Rural Affairs of the People's Republic of China.

Funding: Supported by National Natural Science Foundation of China (32500447), China Postdoctoral Science Foundation (2024M760389 and GZC20230401), Heilongjiang Postdoctoral Fund (LBH-Z24045), and Major Project of Guangzhou National Laboratory (GZNL2023A01001)..

doi: 10.46234/ccdcw2026.027

[#] Corresponding authors: Zhongwei Jia, jiazw@bjmu.edu.cn; Hongliang Chai, Hongliang_chai@hotmail.com.

---

[1] College of Wildlife and Protected Area, Northeast Forestry University, Harbin City, Heilongjiang Province, China; [2] School of Public Health, Peking University, Beijing, China.

Submitted: October 24, 2025
Accepted: February 11, 2026
Issued: February 20, 2026

REFERENCES

1. Harfoot R, Webby RJ. H5 influenza, a global update. J Microbiol 2017;55(3):196 – 203. https://doi.org/10.1007/s12275-017-7062-7.
2. Lewis NS, Banyard AC, Whittard E, Karibayev T, Al Kafagi T, Chvala I, et al. Emergence and spread of novel H5N8, H5N5 and H5N1 clade 2.3.4.4 highly pathogenic avian influenza in 2020. Emerg Microbes Infect 2021;10(1):148-51. http://dx.doi.org/10.1080/22221751.2021.1872355.
3. Leguia M, Garcia-Glaessner A, Muñoz-Saavedra B, Juarez D, Barrera P, Calvo-Mac C, et al. Highly pathogenic avian influenza A (H5N1) in marine mammals and seabirds in Peru. Nat Commun 2023;14(1):5489. https://doi.org/10.1038/s41467-023-41182-0.
4. FAO, WHO, WOAH. Updated joint FAO/WHO/WOAH assessment of recent influenza A(H5N1) virus events in animals and people. 2024. https://cdn.who.int/media/docs/default-source/influenza/avian-and-other-zoonotic-influenza/joint-fao-oie-who-preliminary-risk-assessment-associated-with-avian-influenza-a(h5n1)-virus.pdf?sfvrsn=faa6e47e_28&download=true. [2025-5-14].
5. Plaza PI, Gamarra-Toledo V, Euguí JR, Lambertucci SA. Recent changes in patterns of mammal infection with highly pathogenic avian influenza A(H5N1) virus worldwide. Emerg Infect Dis 2024;30(3): 444 – 52. https://doi.org/10.3201/eid3003.231098.
6. United States Department of Agriculture. Highly pathogenic avian influenza H5N1 genotype B3.13 in dairy cattle: national epidemiologic brief. 2024. https://www.aphis.usda.gov/sites/default/files/hpai-dairy-national-epi-brief.pdf. [2025-6-12].
7. World Organisation for Animal Health. Statement on avian influenza and mammals. 2023. https://www.woah.org/en/statement-on-avian-influenza-and-mammals/. [2025-6-20].
8. World Health Organization. Cumulative number of confirmed human cases for avian influenza A(H5N1) reported to WHO, 2003-2025. 2024. https://cdn.who.int/media/docs/default-source/2021-dha-docs/cumulative-number-of-confirmed-human-cases-for-avian-influenza-a(h5n1)-reported-to-who--2003-2025.pdf. [2025-5-14].
9. Bruno A, Alfaro-Núñez A, de Mora D, Armas R, Olmedo M, Garcés J, et al. First case of human infection with highly pathogenic H5 avian Influenza A virus in South America: A new zoonotic pandemic threat for 2023? J Travel Med 2023;30(5):taad032. http://dx.doi.org/10.1093/jtm/taad032.
10. Centers for Disease Control and Prevention. Risk to people in the United States from highly pathogenic avian influenza A(H5N1) Viruses. 2025. https://www.cdc.gov/cfa-qualitative-assessments/php/data-research/h5-risk-assessment.html. [2025-5-21].
11. Reperant LA, van Amerongen G, van de Bildt MWG, Rimmelzwaan GF, Dobson AP, Osterhaus ADME, et al. Highly pathogenic avian influenza virus (H5N1) infection in red foxes fed infected bird carcasses. Emerg Infect Dis 2008;14(12):1835 – 41. https://doi.org/10.3201/eid1412.080470.
12. Elsmo EJ, Wünschmann A, Beckmen KB, Broughton-Neiswanger LE, Buckles EL, Ellis J, et al. Highly pathogenic avian influenza A(H5N1) virus clade 2.3.4.4b infections in wild terrestrial mammals, United States, 2022. Emerg Infect Dis 2023;29(12):2451-60. http://dx.doi.org/10.3201/eid2912.230464.
13. UK Government. Confirmed findings of avian influenza virus in non-avian wildlife in 2022. 2022. https://www.gov.uk/government/publications/bird-flu-avian-influenza-findings-in-non-avian-wildlife/confirmed-findings-of-influenza-of-avian-origin-in-non-avian-wildlife#confirmed-findings-of-avian-influenza-virus-in-non-avian-wildlife-in-2022. [2025-6-12].
14. European Food Safety Authority, European Centre for Disease Prevention and Control, European Union Reference Laboratory for Avian Influenza, Adlhoch C, Fusaro A, Gonzales JL, et al. Avian influenza overview March-April 2023. EFSA J 2023;21(6):e08039. https://doi.org/10.2903/j.efsa.2023.8039.
15. Chestakova IV, van der Linden A, Bellido Martin B, Caliendo V, Vuong O, Thewessen S, et al. High number of HPAI H5 virus infections and antibodies in wild carnivores in the Netherlands, 2020-2022. Emerg Microbes Infect 2023;12(2):2270068. https://doi.org/10.1080/22221751.2023.2270068.
16. Vreman S, Kik M, Germeraad E, Heutink R, Harders F, Spierenburg M, et al. Zoonotic mutation of highly pathogenic avian influenza H5N1 virus identified in the brain of multiple wild carnivore species. Pathogens 2023;12(2):168. https://doi.org/10.3390/pathogens12020168.
17. Alkie TN, Cox S, Embury-Hyatt C, Stevens B, Pople N, Pybus MJ, et al. Characterization of neurotropic HPAI H5N1 viruses with novel genome constellations and mammalian adaptive mutations in free-living mesocarnivores in Canada. Emerg Microbes Infect 2023;12(1): 2186608. https://doi.org/10.1080/22221751.2023.2186608.
18. USDA. Detections of highly pathogenic avian influenza in mammals. 2026. https://www.aphis.usda.gov/livestock-poultry-disease/avian/avian-influenza/hpai-detections/mammals. [2025-6-15].
19. Agüero M, Monne I, Sánchez A, Zecchin B, Fusaro A, Ruano MJ, et al.

Highly pathogenic avian influenza A(H5N1) virus infection in farmed minks, Spain, October 2022. Euro Surveill 2023;28(3):2300001. https://doi.org/10.2807/1560-7917.ES.2023.28.3.2300001.

20. WOAH. A/H5N1 virus infections in cats. 2023. https://www.woah.org/app/uploads/2023/07/letter-of-polish-cvo-on-cats-en.pdf. [2025-5-16].
21. Frymus T, Belák S, Egberink H, Hofmann-Lehmann R, Marsilio F, Addie DD, et al. Influenza virus infections in cats. Viruses 2021;13(8):1435. https://doi.org/10.3390/v13081435.
22. USDA. Federal and state veterinary agencies share update on HPAI detections in Oregon backyard farm, including first H5N1 detections in swine. 2024. https://www.aphis.usda.gov/news/agency-announcements/federal-state-veterinary-agencies-share-update-hpai-detections-oregon. [2025-5-24].
23. Center for Infectious Disease Research & Policy. Avian flu detected for first time in US livestock. 2024. https://www.cidrap.umn.edu/avian-influenza-bird-flu/avian-flu-detected-first-time-us-livestock. [2025-5-24].
24. USDA. Highly Pathogenic Avian Influenza (HPAI) H5N1 detections in alpacas. 2025. https://www.aphis.usda.gov/livestock-poultry-disease/avian/avian-influenza/hpai-detections/mammals/highly-pathogenic-avian. [2025-5-14].
25. Naraharisetti R, Weinberg M, Stoddard B, Stobierski MG, Dodd KA, Wineland N, et al. Highly pathogenic avian influenza A(H5N1) virus infection of indoor domestic cats within dairy industry worker households-Michigan, May 2024. MMWR Morb Mortal Wkly Rep 2025;74(5):61 – 5. https://doi.org/10.15585/mmwr.mm7405a2.
26. Banyard AC, Bennison A, Byrne AMP, Reid SM, Lynton-Jenkins JG, Mollett B, et al. Detection and spread of high pathogenicity avian influenza virus H5N1 in the Antarctic region. Nat Commun 2024;15(1):7433. https://doi.org/10.1038/s41467-024-51490-8.
27. Puryear W, Sawatzki K, Hill N, Foss A, Stone JJ, Doughty L, et al. Highly pathogenic avian influenza A(H5N1) virus outbreak in New England seals, United States. Emerg Infect Dis 2023;29(4):786 – 91. https://doi.org/10.3201/eid2904.221538.
28. ELOBSERVADOR. Preocupación por 552 lobos marinos muertos a pocos kilómetros del Chuy. 2023. https://www.elobservador.com.uy/nota/preocupacion-por-552-lobos-marinos-muertos-a-pocos-kilometros-del-chuy-20231025183255?utm_source=chatgpt.com. [2025-5-25].
29. Pardo-Roa C, Nelson MI, Ariyama N, Aguayo C, Almonacid LI, Munoz G, et al. 2023. Cross-species transmission and PB2 mammalian adaptations of highly pathogenic avian influenza A/H5N1 viruses in Chile. BioRxiv 2023. http://dx.doi.org/10.1101/2023.06.30.547205.
30. British Antarctic Survey. Antarctica. https://www.bas.ac.uk/about/antarctica/. [2026-2-13].
31. CDC. H5 Bird Flu: current situation. 2026. https://www.cdc.gov/bird-flu/situation-summary/. [2026-2-13].
32. Burrough ER, Magstadt DR, Petersen B, Timmermans SJ, Gauger PC, Zhang JQ, et al. Highly pathogenic avian influenza A(H5N1) clade 2.3.4.4b virus infection in domestic dairy cattle and cats, United States, 2024. Emerg Infect Dis 2024;30(7):1335-43. http://dx.doi.org/10.3201/eid3007.240508.
33. Garg S, Reed C, Davis CT, Uyeki TM, Behravesh CB, Kniss K, et al. Outbreak of Highly Pathogenic Avian Influenza A(H5N1) Viruses in U.S. Dairy Cattle and Detection of Two Human Cases - United States, 2024. MMWR Morb Mortal Wkly Rep. 2024 May 30;73(21):501-505.
34. USDA. USDA announces new federal order, begins national milk testing strategy to address H5N1 in dairy herds. 2024. https://www.aphis.usda.gov/news/agency-announcements/usda-announces-new-federal-order-begins-national-milk-testing-strategy. [2025-12-11].
35. FAO, WHO, WOAH. Updated joint FAO/WHO/WOAH public health assessment of recent influenza A(H5) virus events in animals and people. 2025. https://www.woah.org/app/uploads/2025/04/2025-04-17-fao-woah-who-h5n1-assessment.pdf?utm_source=chatgpt.com. [2025-5-28].
36. CDC. CDC A(H5N1) bird flu response update, July 19, 2024. 2024. https://www.cdc.gov/bird-flu/spotlights/h5n1-response-07192024.html. [2025-5-28].
37. CDC. Current Situation: H5N1 Bird Flu in People. 2025. https://www.cdc.gov/bird-flu/situation-summary/inhumans.html?utm_source=chatgpt.com. [2025-6-11].
38. Guo J, Song WT, Ni XS, Liu W, Wu JW, Xia W, et al. Pathogen change of avian influenza virus in the live poultry market before and after vaccination of poultry in southern China. Virol J 2021;18(1):213. https://doi.org/10.1186/s12985-021-01683-0.

SUPPLEMENTARY MATERIALS

SUPPLEMENTARY TABLE S1. Overall trends of H5N1 infection in mammals (2021–2025, Excluding humans).

Year	Species	Order & Family	Country
2021	Red fox; European mink; Grey seal; Beech marten; Eurasian otter; Eurasian lynx; Domestic pig; European badger; European polecat	Carnivora, Artiodactyla & Canidae, Mustelidae, Felidae, Otariidae, Suidae	Netherlands, Finland, Poland, Estonia, England, Denmark, Scotland, Italy
2022	Red fox; Eurasian otter; Grey seal; Ferret; Harbor seal; Striped skunk; American mink; Raccoon; Coati; European polecat; Virginia opossum; Gray fox; Coyote; Fisher; Bottlenose dolphin; Amur leopard; Amur tiger; American black bear; Grizzly bear; Kodiak bear; Domestic cat; Bobcat; Mountain lion; North American river otter; North American beaver; Dusky dolphin; Atlantic white-sided dolphin; European mink; European badger; Caspian seal; Asiatic black bear; South American sea lion	Carnivora, Cetacea, Rodentia, Didelphimorphia, Artiodactyla & Canidae, Mustelidae, Felidae, Otariidae, Mephitidae, Procyonidae, Didelphidae, Delphinidae, Ursidae, Castoridae, Suidae	Netherlands, England, Ireland, Canada, United States, Japan, Belgium, Slovenia, Germany, Russia, France, Peru, Spain
2023	Red fox; European polecat; Striped skunk; Mountain lion; Domestic cat; Caracal; Bobcat; Raccoon; Harbor seal; Coyote; American black bear; Fisher; Bottlenose dolphin; Polar bear; Abert's squirrel; American mink; Virginia opossum; Amur tiger; Coypu; South American sea lion; Common dolphin; Eurasian otter; Sea otter; Giant otter; Harbor porpoise; Chilean dolphin; Domestic dog; Bush dog; Ferret; Beech marten; Pine marten; Eurasian lynx; Arctic fox; Japanese raccoon dog; South American fur seal; Southern elephant seal; Northern fur seal; Walrus	Carnivora, Cetacea, Rodentia, Didelphimorphia & Canidae, Mustelidae, Felidae, Otariidae, Mephitidae, Procyonidae, Ursidae, Delphinidae, Sciuridae, Echimyidae, Phocoenidae, Odobenidae	United States, Scotland, Wales, Latvia, Finland, Norway, Sweden, Germany, Italy, Belgium, France, Poland, South Korea, Peru, Argentina, Uruguay, Brazil, Chile, Russia, Japan, Antarctica
2024	Domestic cat; Bobcat; House mouse; Red fox; Eurasian otter; Striped skunk; Mountain lion; Raccoon; Bottlenose dolphin; Harbor seal; American black bear; Fisher; American mink; Virginia opossum; Amur tiger; Canada lynx; Eurasian lynx; Geoffroy's cat; Prairie vole; Deer mouse; Muskrat; Desert cottontail; Domestic cattle; Alpaca; Domestic goat; Tiger; Lion; Jaguar	Carnivora, Cetacea, Rodentia, Lagomorpha, Artiodactyla & Canidae, Mustelidae, Felidae, Otariidae, Mephitidae, Procyonidae, Ursidae, Delphinidae, Muridae, Cricetidae, Leporidae, Bovidae, Camelidae	United States, Norway, Peru, Vietnam
2025	Norwegian rat; Deer mouse; Rusty-spotted cat; Canada lynx; House mouse; Striped skunk; Red fox; Harbor seal; Long-tailed weasel; American mink; Bobcat; American black bear; Mountain lion; Black rat; Bottlenose dolphin; Sheep; Eurasian otter; Grey seal	Carnivora, Cetacea, Rodentia, Artiodactyla & Canidae, Mustelidae, Felidae, Otariidae, Mephitidae, Ursidae, Delphinidae, Muridae, Bovidae	United States, Scotland, Germany, England, Wales

Youth Editorial Board

Indexed by Science Citation Index Expanded (SCIE), Social Sciences Citation Index (SSCI), PubMed Central (PMC), Scopus, Chinese Scientific and Technical Papers and Citations, and Chinese Science Citation Database (CSCD)

The inauguration of *China CDC Weekly* is in part supported by Project for Enhancing International Impact of China STM Journals Category D (PIIJ2-D-04-(2018)) of China Association for Science and Technology (CAST).

CHINA CDC WEEKLY

Vol. 8 No. 8 Feb. 20, 2026

CCDC weekly

中国疾病预防控制中心周报（英文）

Responsible Authority
National Disease Control and Prevention Administration

Sponsor
Chinese Center for Disease Control and Prevention

Editor-in-Chief
Jianwei Wang

Editing and Publishing
China CDC Weekly Editorial Office
No.155 Changbai Road, Changping District, Beijing, China
Tel: 86-10-63150501, 63150701
Email: weekly@chinacdc.cn

Printing: Beijing Kexin Printing Co.， Ltd

Complimentary Access

CSSN
ISSN 2096-7071 (Print)
ISSN 2097-3101 (Online)
CN 10-1629/R1